A lithium isotopic perspective of basalt weathering: Cycling of Li and its mobility relative to Ca and Mg		
Anup Kumar Sharma ^{1*} , Tarun Kumar Dalai ¹ , Sambuddha Misra ² , Prem Chand Kisku ³ , Jitendra Kumar Pattanaik ⁴		
¹ Department of Earth Sciences, Indian Institute of Science Education and Research Kolkata, Mohanpur 741246, India		
² Centre for Earth Sciences, Indian Institute of Science, Bangalore 560012, India ³ Council of Scientific and Industrial Research-National Geophysical Research Institute (CSIR-NGRI), Uppal Road, Hyderabad 500007, India		
⁴ Department of Geology, Central University of Punjab, Bathinda, Punjab 151401, India		
*Corresponding author: Anup Kumar Sharma (ak.sharma20795@gmail.com)		

32 Abstract

Lithium isotope composition (δ^7 Li) has been extensively utilized to trace silicate weathering. Although the direction and magnitude of Li isotope fractionation during Li adsorption onto secondary minerals are well understood, the relative importance of Li partitioning via its adsorption vis-à-vis structural incorporation into clay minerals on overall Li isotope fractionation remains poorly constrained. In this study, we investigate the bulk, exchangeable and oxyhydroxide phases of two basaltic weathering profiles to assess the processes regulating Li distribution and its isotope fractionation. The decrease in δ^7 Li values toward the top of the weathering profiles, coupled with increases in Li/Al, Fe/Al, and Mn/Al ratios, indicates role of clay minerals and Fe-Mn oxyhydroxides in the preferential adsorption and/or structural incorporation of δ Li. In one of the profiles, processes of sorption and desorption of Li are driven by pH variations. Mass balance calculations demonstrate that crystal-bound Li in clay minerals dominates the total Li budget of the weathered basalts and therefore drive the depth-dependent variation in δ 7Li within the weathering profiles.

The estimates of $\delta^7 \text{Li}$ in weathering solutions show excellent agreement between two independent approaches. The estimated solution $\delta^7 \text{Li}$ values are about 8.1-12.6‰ higher than that of the parent basalts and fall within the range of $\delta^7 \text{Li}$ offsets observed between the rocks and solutions in river and groundwater systems in basaltic catchments. We establish empirical relationships between $\delta^7 \text{Li}$, mobility of Li relative to Ca and Mg, and the chemical index of alteration (CIA) in weathering profiles. These relationships provide a framework for reliable prediction of $\delta^7 \text{Li}$ and Li mobility relative to Ca and Mg during basaltic weathering. Additionally, by integrating published values of $\delta^7 \text{Li}$ and CIA in river sediments, we demonstrate that $\delta^7 \text{Li}$ values of river sediments can be predicted from their CIA. The results and findings of this study have important implications for the utility of Li isotope composition as a tracer of silicate weathering intensity and the relative mobilities of Li, Ca and Mg.

Keywords

56

57

58

59

60

61

62

63

64

65

66

67

68

69

70

71

72

73

74

75

76

77

78

Basaltic weathering; Lithium isotope; Adsorption; Desorption; pH; Relative mobility

1. Introduction

Chemical weathering of silicate rocks acts as a sink of atmospheric CO₂ over the geological time scale (Walker et al., 1981; Raymo et al., 1988; Amiotte Suchet et al., 2003). Among aerially exposed silicate rocks, basalts represent only ~9% (Rad et al., 2007), whereas their chemical weathering accounts for 30-35% of global CO₂ consumption and contributes to 23-30% of the global dissolved load to sea water (Gaillardet et al., 1999; Dessert et al., 2003; Rad et al., 2007). Lithium and its isotopes have been extensively utilized to study continental silicate weathering (Huh et al., 2001; Dellinger et al., 2015; Pogge von Strandmann and Henderson, 2015) because of several unique features: (i) Li has a relatively uniform crustal distribution in both concentration and isotope space, (ii) it is dominantly hosted in silicate minerals and thus continental weathering flux of Li and its isotopic composition are insensitive to weathering of carbonate rocks, (iii) due to its large relative mass difference, significant isotopic fractionation is observable during incongruent weathering (Pistiner and Henderson, 2003; Rudnick et al., 2004; Misra and Froelich, 2012; Gou et al., 2019). In addition, Li does not participate in biological processes (Pogge von Strandmann et al., 2016). While Li isotopic ratios serve as robust tracers of continental silicate weathering, there is a limited understanding of how Li covaries with Ca and Mg during continental weathering. The mechanistic and quantitative understanding of continental fluxes of two major alkaline earth elements (Ca and Mg) is important because of their intricate involvement in carbon cycle, where their respective carbonate minerals act as the final sink of atmospheric CO₂ over geological time scale (Raymo and Ruddiman, 1992; Gaillardet et al., 1997; Amiotte Suchet et al., 2003; Dessert et al., 2003).

Lithium, the lightest alkali element, is fluid mobile and has two stable isotopes (⁶Li,⁷Li), which have large relative mass difference of ~16%. Thus, significant mass dependent fractionation of Li isotopes

occurs during low temperature water-rock interactions (Chan et al., 1992; Pistiner and Henderson, 2003; Rudnick et al., 2004). The primary cause of Li isotopic fractionation during incongruent weathering has been attributed to equilibrium partitioning of Li between secondary minerals and conjugate fluids (Huh et al., 1998; Pistiner and Henderson, 2003; Vigier et al., 2008). During silicate weathering ⁶Li is preferentially scavenged by the secondary weathering products such as clay minerals and Fe-Mn oxyhydroxides (Chan et al., 1992; Pistiner and Henderson, 2003), whereas the fluid phases are enriched in ⁷Li compared to the secondary solid phases. This phenomenon is attributed to tetrahedral coordination of Li⁺ with four water molecules ([Li(H₂O)₄]⁺), where the weaker hydration bond of ⁶Li-H₂O compared to ⁷Li-H₂O bond (Yamaji et al., 2001; Wimpenny et al., 2015) results in preferential dehydration of ⁶Li leading to its incorporation into octahedral sites of secondary phases (Pistiner and Henderson, 2003; Wimpenny et al., 2010a; Hindshaw et al., 2019). The impact of pH on Li isotopic fractionation has been explored but remains inconclusive (Li and Liu, 2020; Pogge von Strandmann et al., 2012; Zhu et al., 2023). There is no consensus on the direction of Li isotope fractionation with pH variation. For example, Zhu et al. (2023) proposed preferential desorption of ⁶Li at decreasing pH, whereas Li and Liu (2020) documented desorption of ⁷Li under similar conditions. Published body of work on weathering profiles (Lemarchand et al., 2010; Ryu et al., 2014; Chapela Lara et al., 2022) have demonstrated that a decrease in pH in the upper part of the profiles results in the dissolution of secondary phases, leading to a preferential loss of ⁶Li from clay minerals. A few studies also report kinetic fractionation of Li isotopes during low temperature water-rock interactions (Teng et al., 2010). The study of Pistiner and Henderson (2003) demonstrates that the degree of Li isotope fractionation is dependent on the types of secondary minerals, which in turn is influenced by the intensity of weathering.

79

80

81

82

83

84

85

86

87

88

89

90

91

92

93

94

95

96

97

98

99

100

101

Investigation of weathering profiles developed on basaltic rocks have demonstrated that the Li isotope composition of profiles is influenced by secondary mineral formation, external inputs such as the

deposition of marine aerosols and eolian dust, and diffusion of Li across the paleo-water table (Huh et al., 2004; Kısakurek et al., 2004; Rudnick et al., 2004; Teng et al., 2010; Tong et al., 2021; Xiong et al., 2022). Although the magnitude and direction of Li isotopic fractionation during weathering is well understood, there is limited knowledge on the specific processes and their relative importance in regulating δ^7 Li of weathered rocks (Teng et al., 2010). For example, the relative importance of Li adsorption onto clay mineral surfaces vis-a-vis its incorporation into the lattice of neo-formed minerals is poorly understood (Pogge von Strandmann et al., 2010; Wimpenny et al., 2015; Tong et al., 2021; Zhang et al., 2021; Cai et al., 2024; Zhu et al., 2023). Decoupling these processes is crucial for utilizing Li as a tracer of waterparticle interaction during silicate weathering and to develop constraints on fluvial δ^7 Li systematics, which helps us elucidate past and present weathering rates.

We present and discuss Li isotope data of two weathering profiles developed on basaltic rocks of Rajmahal Volcanic Province (RVP) in India. Based on trace element and Li isotope composition of the bulk material and adsorbed fractions of the weathering profiles, we demonstrate that Li isotopes undergo intense cycling after weathering via sorption-desorption processes. Additionally, we evaluate the mobility of Li relative to Ca and Mg during chemical weathering as a function of chemical index of alteration. Utilizing our results and published body of work, we compare relative mobility of Li, Ca and Mg during basalt weathering under variable climate regimes. Furthermore, utilizing published data for riverine suspendered particulate matter (SPM), we demonstrate that δ^7 Li values of SPM can be predicted from their CIA. We also determine Li isotopic composition of weathering solutions using two independent approaches and observe excellent agreement between these calculations.

2. The study area

The Rajmahal Volcanic Province (RVP) is located in central eastern part of India (Fig. 1). The eroded remnants of RVP cover an area of approximately 4300 km² (Ghose et al., 2017). Rajmahal basalts

are mostly exposed in the Rajmahal hills located in the state of Jharkhand. These basalts are made up of multiple volcanic lava flows with a maximum reported thickness of 600 m. These volcanic eruptions are related to the Kerguelen hotspot activity (Baksi, 2022). The rocks are primarily tholeiitic basalts and basaltic andesites, with minor abundances of trachyandesites, andesites, dacites, and rhyolites. The mineral constituents of these basalts are labradoritic plagioclase, pigeonitic-augitic pyroxene, opaque minerals and primary glass (Mukherjee, 1971). The mineral proportions vary, with plagioclase constituting 19–56%, pyroxene 18–47%, and opaque minerals 1–10% of the bulk composition (Mukherjee, 1971).

Rajmahal basalts are dated at 118±2 Myr (Baksi, 2022). The Rajmahal trap basalts were subjected to intense chemical weathering from late Cretaceous to early Paleogene during northward equatorial drift of Indian plate. In peninsular India, the intense chemical weathering along the east-west oriented belt plausibly favored the formation of weathering profiles across the Rajmahal Basalt Traps during the Eocene and Oligocene (Bardossy, 1981). The region currently experiences a humid to sub-humid climate, and receives an annual rainfall of about 1500 mm mostly via southwest monsoon. About 80% of annual rainfall occurs during June to September. The study area is characterized by seasonal rivers flowing from west to east (Fig. 1), many first-order streams, and small tributaries that drain the basaltic terrain, resulting in a characteristic dendritic drainage pattern. The major rivers flowing through this region are the Bansloi, Brahmani and Gumani (Fig. 1).

3. Materials and methods

Two weathering profiles, namely the Dalahi (24° 23.12' N, 87° 28.76' E; Fig. 1) and Pakuria (24° 18.26' N, 87° 45.30' E; Fig. 1), developed on Rajmahal basalts were collected from the southern part of the RVP in Jharkhand, India. Detailed descriptions of these profiles have been given in Sharma et al. (2025). Briefly, the total exposed thickness of the Dalahi and Pakuria profile is ~400 cm and 10 m,

respectively. Both the profiles exhibited gradual upward transitions from basalts to weathered material, followed by a progressively more weathered horizons comprising ferricrete nodules. Our earlier work, based on immobile element ratios, showed that both weathering profiles are well preserved and developed *in-situ* (Sharma et al., 2025). The procedures for glass beads preparation for major elements analysis, sample digestion, and extraction of exchangeable and oxyhydroxide phases are detailed in our earlier publication (Sharma et al., 2025) and briefly summarized in the supplementary material (Section S1).

3.1. Clay-sized fraction

To separate the clay-sized fractions, the residues left after extraction of exchangeable and oxyhydroxide phases (Section 3.2) were treated with a mixture of 30% H_2O_2 and 0.02N HNO₃ to remove the organic fractions (Gupta and Chen, 1975). Thereafter, the clay-sized fractions were separated by centrifugation (Bouchez et al., 2021; Pryor et al., 2024), and their masses were used to calculate clay-sized fractions. The analytical reproducibility, evaluated by replicate determinations, was better than $\pm 4\%$.

3.2. Measurements

The details of measurements of major elements (Al, Ca, Mg, Si, Na, K, Fe, and Mn) and trace elements (Th and Cs) concentrations in bulk samples, as well as Mn concentrations in exchangeable and oxyhydroxide phases are available in Sharma et al. (2025) and briefly summarized in the supplementary material (Section S2). The new data generated in this study include Li concentrations in bulk, concentrations of Li, Ba, Al and Cs in exchangeable and oxyhydroxide phases, and δ^7 Li values in bulk rocks and weathered materials.

The bulk Li concentrations were determined by analyzing the acid-digested solutions by a quadrupole ICP-MS (Thermoscientific® X Series 2) at IISER Kolkata following multi-element external calibration and internal standard (In) addition. The measurement accuracy was better than $\pm 7\%$ as determined from analysis of multiple certified reference standards like BHVO-2 (Hawaiian Basalt), GSP-

2 (Granodiorite), and JSD-3 (Stream sediment) (Table S1). The analytical reproducibility, based on replicate analyses, was within $\pm 2\%$.

The concentrations of Li, Cs, Ba, and Al in the exchangeable and oxyhydroxide fractions were determined using a quadrupole ICP-MS (Thermoscientific® X Series 2) at IISER Kolkata following multi-element external calibration and internal standard (In) addition. The measurement accuracy, based on analysis of certified reference standard BHVO-2 and NIST-traceable standard IV-Stock 8 (Inorganic Ventures®), was better than $\pm 3\%$ for Li and Ba, and $\pm 7\%$ for Al and Cs (Table S2). Analytical reproducibility, evaluated based on replicate analyses, was within $\pm 8\%$ for all elements in both the exchangeable and oxyhydroxide phases.

3.2.1. Li purification and δ^7 Li analysis

Lithium was purified following the method outlined by Bohlin et al. (2018). The Savillex® PFA columns with an inner diameter of 4 mm and a height of 25 cm were packed with 3 mL of Bio-Rad® AG MP-50 cation exchange resin (100–200 μm mesh size). The resin was cleaned with 10N HCl, followed by Milli-Q water wash. The resin was allowed to resettle by gravity, ensuring a uniform resin bed. The column was then conditioned with 9 mL of 0.7N HCl. Samples solutions containing 1-2 ng of Li were loaded onto the resin in 200 μL of 0.7N HCl. The columns were washed with 3 mL of 0.5N HF, followed by 8 mL of 0.7N HCl. Lithium was then eluted using 13 mL of 0.7N HCl. To ensure complete recovery and account for any potential tailing of the Li peak, 1 mL fractions were collected both before and after the Li cut. The purified Li-aliquots were collected in acid-cleaned Savillex® vials and dried overnight on a hotplate at 80°C. After drying, the samples were refluxed for 24 hours with 200 μL of concentrated HNO3 to dissolve residual organic matter, if any. After refluxing, the solutions were evaporated to dryness and re-dissolved in 200 μL of 2% HNO3 prior to isotope analysis. All acids (HNO3, HCl, and HF) used for column chromatography and Li isotope analysis were purified by double distillation using a Savillex®

DST-4000 sub-boiling distillation unit in a ISO Class 5 (Class 1000) laminar flow clean bench, placed within an ISO Class 7 (Class 10000) cleanroom.

Lithium isotope ratio was determined using a single collector triple quadrupole ICP-MS (Agilent® 8900) at IISc Bangalore (Juzer et al., 2022). Instrumental mass bias was corrected using external normalization following the standard sample bracketing (SSB) protocol (Bohlin et al., 2018) with Li concentration matching of all samples with NIST-L-SVEC-8545 standard. Samples were analyzed at [Li] of 0.8 ppb using a block of 75 cycles, with integration time of 2.6 seconds for ⁶Li and 0.2 seconds for ⁷Li. Measurements were done in duplicate, and both isotopes were determined in pulse mode. The results are reported as δ⁷Li (‰), calculated using the formula [{(⁷Li/⁶Li)_{Sample}/(⁷Li/⁶Li)_{Standard} -1} ×1000]‰, with NIST-L-SVEC-8545 as the reference standard. The measured δ^7 Li of the rock standards BCR-2 and BHVO-2 were $3.30\pm0.58\%$ (2 σ ; n=2) and $4.44\pm0.96\%$ (2 σ ; n=2), respectively. These values are analytically indistinguishable from published values of BCR-2: 3.19 ±0.39‰ and BHVO-2: 4.58±0.38‰ (Zhu et al., 2019). Purification and analysis of seawater yielded a δ^7 Li value of 31.26±0.82‰ (2 σ ; n=3) which is in good agreement with the published values of 31.27±0.4‰ (Bohlin et al., 2018; Juzer et al., 2022). The measured δ^7 Li value for the secondary Li standard (6Li-N-SRM) is $-8.27 \pm 0.40\%$ (2 σ ; n = 3), which is within the range of published values of $-8.18 \pm 0.39\%$ (Bohlin et al., 2018). Analysis of samples in replicates provides the mean external reproducibility of the measured δ^7 Li to be $\pm 0.24\%$ (2 σ , n=4).

4. Results

194

195

196

197

198

199

200

201

202

203

204

205

206

207

208

209

210

211

212

213

214

215

The concentrations of major and trace elements in the weathered materials and parent basalts are listed in Table 1. The density and pH data are listed in Table 1. The concentrations of Ca, Na and Mg decrease (Table 1), while the concentrations of Al, Fe and Mn increase toward the top of the profiles (Table 1).

The elemental loss during the chemical weathering was determined relative to the parent basalt by normalizing concentrations of an element to that of the immobile element Th (Nesbitt, 1979):

$$[m]_{lost} \% = \left[1 - \left(\frac{\left(\frac{C_{m,w}}{C_{l,w}}\right)}{\left(\frac{C_{m,p}}{C_{l,p}}\right)}\right)\right] \times 100 \tag{1}$$

where C is concentration of a mobile (m) or immobile (i) element in the weathered materials (w) or parent (p) basalts. Thorium (Th) is used as an immobile element because it behaves conservatively during the weathering of basalt (Ma et al., 2007), and show minimal contribution from aeolian dust sources in these weathering profiles (Sharma et al., 2025). An elemental gain or loss relative to the parent rock composition is implied if $[m]_{lost}$ % < 0 or > 0, respectively. The upward increase in $[Li]_{lost}$ % in both profiles, associated with the increasing CIA values (Fig. 2), suggests Li loss due to weathering of primary minerals. However, in the Dalahi profile, the $[Li]_{lost}$ % exhibits an upward decrease starting at ~110 cm, indicating significant Li enrichment in the top section.

4.1. Lithium concentrations and δ^7 Li values in weathering profiles

In the unaltered basalts (parent), Li concentrations range from 5.4 to 6.3 μ g/g, and δ^7 Li values vary from 6.1 to 8.1% (Table 1). These [Li] values are identical to published data for basalts (Huh et al., 2004; Liu et al., 2013; Xiong et al., 2022), whereas the δ^7 Li values of the Rajmahal basalts are similar to the upper limits of δ^7 Li values reported for the Hawaiian basalts (4‰–6‰; Pistiner and Henderson, 2003; Huh et al., 2004), Hainan basalts (0.7‰–5.3‰; Xiong et al., 2022), but higher than those in the Deccan basalts (2.5‰; Kisakurek et al., 2004). In weathered materials of the two studied profiles, [Li] and δ^7 Li values vary significantly, ranging from 4.1 to 14.4 μ g/g and 0.5 to 6.9‰, respectively (Table 1). The higher [Li] was observed in the upper sections of both the profiles followed by a gradual downward decrease (Table 1). In Dalahi profile, the δ^7 Li value increases downward from 2.1‰ at the top up to a

value of 5.1‰ at ~80 cm depth. In the section deeper than 80 cm, δ^7 Li values decrease to a value of 0.9‰ at ~130 cm depth (Table 1; Fig. 2). Further below, δ^7 Li values increase downward up to the parent rock values. In Pakuria profile, the δ^7 Li value decreases from 3.1‰ at the top to 0.5‰ at 165 cm, followed by an increasing downward variation up to the basaltic values.

4.2. Elemental composition of leachable phases

The concentrations of major and trace elements in the exchangeable and oxyhydroxide phases are listed in Table 2. The concentrations of Li, Mn, and Al are higher in the oxyhydroxide fractions than in the exchangeable fractions, whereas concentrations of Ba exhibit an opposite trend (Table 2). The cumulative elemental concentrations of both exchangeable and oxyhydroxide fractions are considered here as representative of the adsorbed ([]ads) fraction. In Dalahi profile, [Li]ads increases upward up to 60 cm, before decreasing towards the top (Table 2), whereas in the Pakuria profile, [Li]ads shows an upwardly increasing trend (Table 2). Significant positive correlations of [Li/Al]ads and [Ba/Al]ads with [Mn/Al]ads and [Cs/Al]ads (Fig. S1) indicate that [Li]ads and [Ba]ads are associated with clay minerals and Mn oxyhydroxides in both the profiles. These observations are consistent with the knowledge that clay minerals and oxyhydroxides are efficient in adsorbing both Li and Ba (Eylem et al., 1990; Chan and Hein, 2007; Pogge von Strandmann et al., 2023; Sajih et al., 2014; Cai et al., 2024; Zhu et al., 2023).

5. Discussion

5.1. Potential Li and δ^7 Li contribution from aeolian dust

The preservation and *in-situ* nature of the Dalahi and Pakuria profiles were evaluated by Sharma et al. (2025) through detailed analyses of major and trace element compositions. Based on the variation of Nb and Zr, Sharma et al. (2025) estimated that aeolian dust accounts for up to \sim 5% and \sim 7% of total mass in the Dalahi and Pakuria profiles, respectively. The mass flux of Li derived from dust (F_{Li}^{dust}) in each

sample was calculated following the approach of Kurtz et al. (2001), using the mass fraction of dust (f_d)
estimated based on the Nb–Zr pair (Sharma et al., 2025) and the Li concentration of the UCC (20 µg/g;
Taylor and McLennan, 1985) as the dust endmember (C_{Li}^{dust}):

$$F_{Li}^{dust}(mg/cm^2) = \sum f_d \times C_{Li}^{dust} \times \rho_i \times \Delta t_i \times 10^{-3}$$
 (2)

where ρ_i is the density of a section i (g/cm³) with a thickness Δt_i (cm). The estimated mass flux of Li derived from aeolian dust are 0.13 mg/cm² and 0.26 mg/cm² in the Dalahi and Pakuria profile, respectively. The mass flux of Li released from the weathering of basalt is calculated using the method outlined by Ryu et al. (2014):

$$F_{Li}^{basalt}(mg/cm^2) = C_{Li}^p \times Z_t \times S_c \times \rho_p \times 10^{-3}$$
(3)

where C_{Li}^P is the Li concentration in the parent basalts (5.39-6.26 µg/g, Table 1). The profile thickness (Z_t) is 376 cm in Dalahi and 1000 cm in Pakuria profile (Table 3). The collapse factor (S_c) is defined as the ratio of Th in topmost weathered material to basalt and is used to correct for mass loss or gain during weathering (2.54-2.84, Table 3). The basalt density (ρ_p) is 2.26 and 2.58 g/cm³ for the Dalahi and Pakuria profile (Table 1), respectively. The calculated mass flux of Li (F_{Li}^{basalt}) ranges from 11.65 mg/cm² and 45.76 mg/cm² in the Dalahi and Pakuria profile, respectively. This suggest that the Li mass flux derived from dust is insignificant, accounting for <0.6% in the Pakuria and <1.2% in Dalahi profile (Table 3).

The impact of dust on the bulk $\delta^7 Li$ of weathered materials was evaluated by using a two-component mixing model:

$$\delta^{7} \text{Li}^{\text{expected}} = \delta^{7} \text{Li}^{\text{dust}} f_{\text{Li}}^{\text{dust}} + \delta^{7} \text{Li}^{\text{P}} \left(1 - f_{\text{Li}}^{\text{dust}} \right)$$
 (4)

Using the fraction of Li derived from dust (f_{Li}^{dust} ; Table 3) and the δ^7 Li composition of the UCC (0.6%; Sauzeat et al., 2015) as the dust endmember (δ^7 Li dust), we show that dust input can lower δ^7 Li values

relative to the parent basalt ($\Delta \delta^7 \text{Li}^{P-\text{expected}}$) by up to 0.04‰ in Pakuria and 0.06‰ in Dalahi profile. Therefore, the dust-induced decrease in $\delta^7 \text{Li}$ values is insignificant, given that the $\delta^7 \text{Li}$ differences between parent basalt (P) and weathered materials ($\Delta \delta^7 \text{Li}^{P-\text{bulk}}$) are up to 5.3‰ in Dalahi and 7.7‰ in Pakuria profile. However, if the Saharan dust compositions ([Li]=18.5 µg/g; $\delta^7 \text{Li}=-0.7$ ‰, Clergue et al., 2015) are used, the dust-induced decrease in $\delta^7 \text{Li}$ values relative to the parent basalt is 0.05‰ in Pakuria and 0.07‰ in Dalahi profile. Our exercise demonstrates that dust derived Li has an insignificant impact on [Li] and $\delta^7 \text{Li}$ in the profiles, irrespective of the end member dust compositions used in calculations.

5.2. Cycling of Li during progressive weathering: relative role of adsorption vs. structural incorporation

The loss of major cations due to the breakdown of minerals during chemical weathering is evident from the upward decreasing trends in Ca/Al, Na/Al, Si/Al and Mg/Al ratios for both the profiles (Fig. 2). The evidence for progressive weathering of minerals also comes from increasing trends in the chemical index of alteration (CIA) in the upward direction for both profiles (Fig. 2). The upward increase of [Li]_{lost} % in both profiles, associated with the increasing CIA values (Fig. 2), suggests a loss of Li due to weathering of primary minerals. These observations suggest that the increase in weathering intensity in the upper sections of profiles is characterized by a greater degree of elemental loss from primary minerals such as plagioclase and pyroxene. However, in Dalahi profile, [Li]_{lost} % exhibits an upward decrease starting at ~110 cm, implying addition of Li. Additionally, Li/Al, Fe/Al and Mn/Al ratios exhibit increasing upward trends, supporting the notion of Li addition to the profile through secondary phases such as clay minerals and Fe-Mn oxyhydroxides (Fig. 2). The Li addition can result from any one or a combination of the following processes: (i) adsorption of Li onto the surfaces of clay minerals and Fe-Mn oxyhydroxides, and (ii) Li incorporation into the crystal structure of neo-formed clay minerals. Lithium

is known to be adsorbed onto secondary phases, which is also evident from observed moderate to high positive correlations of Li/Al with Mn/Al, Al/Si and Fe/Al in the weathering profiles (Fig. 3a-c), indicating its adsorption onto clay minerals and Fe-Mn oxyhydroxide phases. Furthermore, Li/Al ratios demonstrate strong positive correlation with Cs/Al, thus providing further evidence for Li sorption in the profiles (Fig. 3d). Because of its large size, Cs is strongly adsorbed onto clay minerals (Nesbitt et al., 1980; Kabata-Pendias and Pendias, 2001) and therefore is used here as an index of adsorption (Sharma et al., 2025). However, the compositions of leachable phases (exchangeable and oxyhydroxides) show that adsorbed Li accounts for only <5% of the bulk Li. Moreover, the upward increase in Al/Si ratios and clay-sized fractions (Tables 1 and 2) raises the possibility that clay minerals also incorporate a substantial amount of Li into their crystal structure. We test this possibility using mass balance calculations (Section S3, supplementary information), which demonstrate that a majority of Li in the bulk phases is hosted within the crystal structures of the neo-formed clay minerals ([Li]_{crystal-bound}), accounting for up to ~85-90% of total Li (Section S3 and Table S3). These results are consistent with the study of Pogge von Strandmann et al. (2019), which demonstrated that up to 84–88% of Li is incorporated into the crystal lattice of newly formed clay minerals, with a minor fraction being adsorbed onto mineral surfaces.

302

303

304

305

306

307

308

309

310

311

312

313

314

315

316

317

318

319

320

321

322

323

324

The calculated crystal-bound molar Al/Si ratios of clay minerals vary from 0.41 to 0.84 (Section S3; Table S3) in the studied profiles, and increase toward the top of the profiles with an increase in weathering intensity (Table S3, Fig. S2a). This upward increase in Al/Si ratio indicates progressive desilication and formation of Al-rich clay minerals such as kaolinite (Delvigne et al., 2016; Frings et al., 2021). The range of calculated Al/Si ratios corresponds to mixed assemblages of clay minerals consisting of montmorillonite (Al/Si: 0.33 to 0.50, Rozalen et al., 2009; Khalifa et al., 2020), illite (Al/Si: 0.79, Khalifa et al., 2020), and kaolinite (Al/Si: 0.92 to 0.95, Frings et al., 2021). Furthermore, the positive correlation between molar Al/Si ratio and [Li]_{crystal-bound} (Fig. S2b) suggests that, clay minerals such as

kaolinite formed during progressive weathering drive enhanced incorporation of Li into their crystal structures.

5.3. Variation of δ^7 Li and influence of post-weathering processes

In the upper layers of the profiles, $\delta^7 \text{Li}$ values exhibit considerable fluctuations and are lower than the basaltic $\delta^7 \text{Li}$ values (Fig. 2). Additionally, $\delta^7 \text{Li}$ values show weak to significant positive correlations with CIA, Mg/Al, Ca/Al and Na/Al ratios (Fig. S3). As Li isotopes do not fractionate during dissolution (weathering) of silicate minerals (Pistiner and Henderson, 2003; Huh et al., 2004), the $\delta^7 \text{Li}$ variation is likely driven by post-weathering processes. As discussed earlier, sorptive enrichment of Li is evident in the upper sections of both profiles. The lower $\delta^7 \text{Li}$ values in the upper sections of the profiles are driven by either adsorption of Li or its incorporation into structure of neo-formed clay minerals (Pistiner and Henderson, 2003; Lemarchand et al., 2010; Hindshaw et al., 2019; Li and Liu, 2020; Chapela Lara et al., 2022) or both. Further evidence for the role of secondary minerals come from inverse correlations of $\delta^7 \text{Li}$ with Al/Si, Cs/Al ratios and adsorbed Mn concentrations ([Mn]_{ads}) (Fig. 4). These observations together support the hypothesis that post weathering processes of basalts play a crucial role in regulating the $\delta^7 \text{Li}$ values in weathering profiles, as observed elsewhere for basaltic weathering (Huh et al., 2004; Kısakurek et al., 2004; Tong et al., 2021; Xiong et al., 2022).

5.4. The effect of pH on geochemical cycling of Li and its isotopic composition

The degree of Li loss ([Li]_{lost}%) varies considerably with depth and exhibits general upward increasing trends in both profiles (Fig. 2). However, as discussed earlier, in the upper ~110 cm of the Dalahi profile, [Li]_{lost}% is characterized by an upwardly decreasing trend (Fig. 2), indicative of enrichment of Li. This observation, together with a ~2-fold increase in the Al/Si ratio and increase in clay-sized fraction (%) in the upward direction (Tables 1 and 2) in this section of the upper Dalahi profile, is

supportive of incorporation of substantial amount of Li into crystal structure of the clay minerals (Section S3). The δ^7 Li values in both profiles decrease from the bottom to the top (Fig. 2), except in the upper 130 cm of the Dalahi profile, where its fluctuations define a boomerang-shaped pattern. Furthermore, the δ^7 Li values in this profile increase downward within the depth interval of 32-80 cm followed by a downward decrease up to a depth of 130 cm. These patterns indicate that heavier Li (7 Li) desorbed from upper horizon of the profile is transported downward by 7 Li rich pore water and is subsequently re-adsorbed by the underlying horizon. Given that 7 Li is preferentially released during desorption, this process can account for at least a part of the observed δ^7 Li increase up to a depth of 130 cm in the Dalahi profile.

347

348

349

350

351

352

353

354

355

356

357

358

359

360

361

362

363

364

365

366

367

368

369

The distribution of Li and fractionation of its isotopes in weathering profiles are known to be modulated by variation of pH (Lemarchand et al., 2010; Zhu et al., 2023; Chapela Lara et al., 2022). Experimental studies show that Li is partitioned between interlayer and octahedral sites of clay minerals, with octahedral sites preferentially being enriched in ⁶Li (Wimpenny et al., 2015; Hindshaw et al., 2019). The distribution of Li isotopes between interlayer and octahedral sites can cause a difference of ~20% in δ^7 Li (Williams and Hervig, 2005; Vigier et al., 2008). In basaltic weathering profile, δ^7 Li of exchangeable phase has been reported to be up to $\sim 20\%$ heavier than that of residual phase (Tong et al., 2021). Published body of work on clay minerals shows that a decrease in pH of equilibrating solution promotes the release of Li from exchangeable sites (Hao et al., 2021). However, the exact mechanism(s) responsible for the pH-driven Li isotope fractionation remains enigmatic. The striking similarity between the upward decreasing trends of $\delta^7 \text{Li}$, [Li]_{ads} and pH in the upper ~80 cm of the Dalahi profile (Fig. 5) is suggestive of δ^7 Li variation in this section through pH dependent processes. Specifically, our data indicates desorption of Li at lower pH in the upper ~80 cm of profile, leading to preferential release of ⁷Li from interlayer sites. This inference is in line with the observations of (i) up to ~28% higher δ^7 Li values of the exchangeable phases than that of crystal-bound Li in clay minerals in a weathering profile developed on

paragneiss (Cai et al., 2024) and (ii) preferential leaching of ⁷Li from interlayer sites of clay minerals during granite weathering, resulting in ⁶Li enrichment of residual Li in weathered materials (Zhang et al., 2021). Our hypothesis of pH dependent desorption of Li is further supported by experimental studies that demonstrate preferential desorption of ⁷Li when pH of the reacting solution was decreased from 8.5 to 4.3 (Li and Liu, 2020).

370

371

372

373

374

375

376

377

378

379

380

381

382

383

384

385

386

387

388

389

390

391

392

The desorption of Li in upper ~80 cm of the Dalahi profile is likely driven by the adsorption of Al, as evident from an increase of [Al]_{ads} towards top of the profile with a decrease in soil pH (Fig. 5). Published body of work has reported that Al³⁺ becomes the dominant cation in the interlayer sites of the clay minerals as soil pH decreases (Jin et al., 2010). Furthermore, the pH-dependent desorption of Li from the upper section also finds support from a positive correlation of [Ba]_{ads} with [Li]_{ads} in lower part of the profile and a [Ba]_{ads} – [Li]_{ads} negative correlation in upper part of the Dalahi profile (Fig. 6). Here, we use Ba as a pH-independent tracer, as its adsorption-desorption is known to be insignificantly impacted by pH variations (Eylem et al., 1990; Zhang et al 2001). The adsorption of Ba is evident in significant positive correlations of [Ba]_{ads} and clay-sized fractions with Al/Si ratio (Fig. 6), suggesting that degree of Ba adsorption increases with the abundance of clay minerals. Furthermore, the positive correlation of [Li]_{crystal-bound} with [Li]_{ads} in the lower section below ~80 cm and the negative correlation in upper section (Fig. 6). These observations together support the idea that in upper section, Li is getting desorbed, while it is added to the crystal structures as evident from upward increasing trend of [Li]_{crystal-bound} enriched in ⁶Li (Table S3). Furthermore, [Li/Al]_{ads} ratios show a positive correlation with pH, whereas [Li/Al]_{crystal}bound ratios do not exhibit such a correlation (Fig. S4). This observation is in line with the knowledge that Li adsorption onto or its desorption from clays surfaces is influenced by pH (Park et al., 2015; Prodromou, 2016; Li and Liu, 2020), while incorporation of Li into the crystal structure of clay minerals is independent of pH variation (Hoyer et al., 2015).

It is noteworthy that our inference of Li desorption in the upper section is not evident from the decreasing trend of bulk Li/Al in downward direction (Fig. 1), although the observed δ^7 Li variation is consistent with this interpretation. This apparent discrepancy can be reconciled with the analytical resolution of concentration determination, which limits our ability to delineate these trends. On the contrary, the change of δ^7 Li associated with desorption can be discerned because of higher analytical precision of δ^7 Li and significant δ^7 Li differences between the adsorbed and [Li]_{crystal-bound} in neo-formed clay minerals (up to ~28‰; Tong et al., 2021; Cai et al., 2024). It is noteworthy that a strong negative correlation is observed between $\Delta\delta^7$ Li_{bulk-crystal bound} and the fraction of crystal-bound Li ($f_{Li}^{crystal-bound}$) in clay minerals (Fig. S5), suggesting that with an increase in the fraction of [Li]_{crystal-bound}, the $\Delta\delta^7$ Li_{bulk-crystal-bound} decreases (See Section S4 for δ^7 Li_{crystal-bound} calculations, Fig. S5). These results further underline the importance of crystal-bound Li in influencing the bulk δ^7 Li values in weathered basalts.

Our inference of Li desorption and the resultant decrease in δ^7 Li values within the top 80 cm layer of the Dalahi profile is consistent with signatures of re-adsorbed Li in the layer below, as evident from an increasing trend in upward direction (130-80 cm) of [Li]_{ads}%, δ^7 Li values, and pH (Fig. 4). The observations shown in Fig. 4 indicate that below the zone of Li desorption, ⁷Li-enriched porewater migrates downward that drives re-adsorption of Li at higher pH. This is expected because, the degree of Li adsorption increases at higher pH (Park et al., 2015; Prodromou, 2016; Li and Liu, 2020). Thus, our interpretation of pH-dependent Li desorption and re-sorption are consistent with the established behavior of Li in surficial aqueous environments.

5.5. Modeling Li isotopic fractionation

As discussed above, the general decreasing trends in δ^7 Li values observed in both profiles are dominantly driven by the preferential incorporation of 6 Li into the structure of clay minerals (Pistiner and

Henderson, 2003; Hindshaw et al., 2019; Li and Liu, 2020). The Rayleigh fractionation model has been previously applied to explain the δ^7 Li variations in weathering profiles (Rudnick et al., 2004; Liu et al., 2013). However, because Li transport in weathering profiles occurs primarily via ionic diffusion rather than via advection, δ^7 Li variations can be accurately explained using a batch fractionation model (Teng et al., 2010; Bouchez et al., 2013; Clergue et al., 2015; Negrel and Millot, 2019). We incorporate batch fractionation model (Bouchez et al., 2013; Clergue et al., 2015; Negrel and Millot, 2019) into a two-step scenario to predict the evolution of δ^7 Li values in two weathering profiles. The first step involves the release of Li during dissolution of the parent rock without any isotopic fractionation (Pistiner and Henderson, 2003). The second step involves the preferential incorporation of δ Li from solution into the crystal-structure of clay minerals. This process has an apparent fractionation factor of α [α _{solid-solution}= (7 Li/ 6 Li)_{solid}/(7 Li/ 6 Li)_{solution}] usually less than 1. We assume isotopic equilibrium between the solution and the secondary phases during Li incorporation. Therefore,

$$\delta^{7} \text{Li}_{w} = \frac{\alpha_{\text{solid-solution}} \times \delta^{7} \text{Li}_{p} + 1000 f_{\text{Li}} \times (\alpha_{\text{solid-solution}} - 1)}{\alpha_{\text{solid-solution1}} (1 - f_{\text{Li}}) + f_{\text{Li}}}$$
 (5)

where w and p refer to weathered materials and parent basalt, respectively. The fraction of Li incorporated into secondary phases (1- f_{Li}) can be determined, relative to the immobile element Th, as the following:

$$1-f_{Li} = \frac{\left(\frac{Li}{Th}\right)_{w}}{\left(\frac{Li}{Th}\right)_{p}} \tag{6}$$

The optimal fractionation factors for the profiles were determined based on the best fit of the model data with the measured δ^7 Li values. The optimal fractionation factors ($\alpha_{solid-solution}$) range from 0.980 to 0.998 and 0.971 to 0.994 for Dalahi and Pakuria profile (Fig. 7), respectively. These $\alpha_{solid-solution}$ values are

consistent with those either determined experimentally ($\alpha_{solid-solution} = 0.972-0.999$; Wimpenny et al., 2015 and references therein), or obtained from field studies ($\alpha_{solid-solution} = 0.970-0.989$; Millot et al., 2010; Tipper et al., 2012; Dellinger et al., 2015; Clergue et al., 2015; Negrel and Millot, 2019). The large range in optimal $\alpha_{solid-solution}$ (Fig. 7) suggests that the evolution of δ^7 Li in the weathering profiles is most likely influenced by the nature of secondary minerals (See section 5.2), given that the magnitude of Li isotope fractionation varies significantly with the type of secondary phase (Vigier, 2008; Wimpenny et al., 2015). For example, Wimpenny et al. (2015) reported a $\alpha_{solid-solution}$ value of 0.984 for Li incorporation into structure of gibbsite, whereas Vigier (2008) reported $\alpha_{solid-solution}$ values of 0.979-0.988 for Li incorporation into the smectite structure. Our calculations indicate that batch fractionation model can effectively explain the range of δ^7 Li values in the entire weathered sections in both the Dalahi and Pakuria profiles, except for four samples (RJS-3, RJS-4, RJS-5, and RJS-6) in the upper part of the Dalahi profile. As discussed earlier in section 5.4, the δ^7 Li signatures of these samples are influenced by Li desorption.

5.6. Calculation of Li isotopic composition of weathering solutions

The Li isotopic composition of weathering solutions reflects the extent of water-rock interaction, the magnitude and direction of Li isotopic fractionation, thereby provide an understanding of Li mobility. Since Li is partitioned between the fluid and solid phases during and after weathering, the δ^7 Li of the solution provides insights into the relative contributions of primary mineral dissolution, secondary mineral formation, and adsorption/desorption processes. Here, we determine the δ^7 Li value of solutions, based on the premise that Li behaves conservatively during weathering and thus the total Li distributed between the weathering solution and the weathered material is equivalent to parent rock. Therefore, the following relationship can be written:

$$f_{Li}^{sol} + f_{Li}^{profile} = 1 \tag{7}$$

$$\delta^{7} \text{Li}_{p} = (f_{\text{Li}}^{\text{sol}} \times \delta^{7} \text{Li}_{\text{sol}}) + (f_{\text{Li}}^{\text{profile}} \times \delta^{7} \text{Li}_{\text{profile}})$$
(8)

where the $\delta^7 \text{Li}_p$, $\delta^7 \text{Li}_{sol}$ and $\delta^7 \text{Li}_{profile}$ represent average $\delta^7 \text{Li}$ of fresh basalt (parent), solution and weathering profile, respectively, f represents the fraction of Li in solution (f_{Li}^{sol}) or in weathering profile ($f_{Li}^{profile}$) relative to parent rock. Therefore,

$$\delta^{7} \text{Li}_{\text{sol}} = \left[\frac{\delta^{7} \text{Li}_{p} - \left(f_{\text{Li}}^{\text{profile}} \times \delta^{7} \text{Li}_{\text{profile}} \right)}{\left(1 - f_{\text{Li}}^{\text{profile}} \right)} \right]$$
(9)

The fraction of Li in the whole profile can be estimated from the mass balance of Li:

462
$$f_{Li}^{profile} = \frac{\left(\frac{\sum_{i=1}^{n}[Li]_{i}\times\Delta t_{i}\times\rho_{i}}{\sum_{i=1}^{n}[Th]_{i}\times\Delta t_{i}\times\rho_{i}}\right)}{\left(\frac{Li}{Th}\right)_{p}}$$
(10)

where ρ_i and Δt_i represent the density and thickness of any sampling section (i), respectively. Similarly, depth integrated $\delta^7 \text{Li}_{\text{profile}}$ of the whole profile can be calculated as:

$$\delta^{7} \text{Li}_{\text{profile}} = \frac{\sum_{i=1}^{n} \delta^{7} \text{Li}_{i} \times [\text{Li}]_{i} \times \Delta t_{i} \times \rho_{i}}{\sum_{i=1}^{n} [\text{Li}]_{i} \times \Delta t_{i} \times \rho_{i}}$$
(11)

The $\delta^7 Li_{sol}$ calculated based on eq. 9 are 14.9±2.1‰ and 20.8±4.4‰ for the Dalahi and Pakuria profiles, respectively. The $\delta^7 Li_{sol}$ can be independently determined using the fractionation factor (α) used earlier in the batch fractionation model.

$$\delta^{7} \text{Li}_{\text{sol}} = (1 - \alpha_{\text{solution-solid}}) \times 1000 + \delta^{7} \text{Li}_{p}$$
 (12)

Using the average values of α (0.991±0.007 for the Dalahi and 0.985±0.008 for Pakuria profiles, Fig. 7) and $\delta^7 \text{Li}_p$ (6.13‰-8.14‰; Table 1) in the eq. 12, the $\delta^7 \text{Li}_{sol}$ is calculated to be 15.1‰ for the Dalahi profile and 23.1‰ for the Pakuria profile. The $\delta^7 \text{Li}_{sol}$ calculated based on two independent approaches are indistinguishable from each other considering errors of determination. The $\Delta\delta^7 \text{Li}_{parent-sol}$ for two profiles

(-8.1 to -12.6‰) fall between the $\Delta\delta^7 \text{Li}_{\text{parent-sol}}$ values reported for groundwaters (-5.6 to -20.3‰) and rivers (-7.7 to -29.5‰) draining the basaltic catchments (Fig. S6; Pogge von Strandmann et al., 2006; Liu et al., 2015), providing further confidence in our determination of $\delta^7 \text{Li}_{\text{sol}}$ values.

5.7. Mobility of Li relative to Ca and Mg during basalt weathering

474

475

476

477

478

479

480

481

482

483

484

485

486

487

488

489

490

491

492

493

494

495

496

The variation of global atmospheric CO₂ levels over the geological time scale depends on the mechanism and rates of silicate weathering (Raymo and Ruddiman, 1992; Gaillardet et al., 1997; Amiotte Suchet et al., 2003; Dessert et al., 2003; Misra and Froelich, 2012). Lithium isotope composition of rivers is considered a reliable tracer of silicate weathering, as dissolved Li is primally sourced from weathering of silicate minerals (Dellinger et al. 2015; Gou et al. 2019, Pogge von Strandmann et al., 2020). For meaningful utilization of [Li] and δ^7 Li as tracers of silicate weathering, it is important to establish the relationships between Li and Ca (Mg) during weathering, given that the precipitation of both Ca and Mg as carbonate minerals in seawater impacts the long-term CO₂ budget of the atmosphere. Thus, mobility of Li relative to Ca and Mg during weathering has been of interest in recent studies (Pogge von Strandmann et al., 2016; 2017a; 2019; 2020). The relative mobility of Li compared to Ca and Mg is reported in studies based on river water compositions (Dellinger et al., 2015; Pogge von Strandmann et al., 2016; 2017b; 2020); however, relative behaviour of these elements during weathering remains unaddressed. The formation of clay minerals and oxyhydroxides during weathering and transport can sequester substantial amount of Ca, and Mg, thereby affecting the efficiency of silicate weathering in drawing down the CO₂ (Dellinger et al., 2015; Pogge von Strandmann et al., 2017a; Pogge von Strandmann et al., 2019; Tipper et al., 2021). The observed trend of Li/Al ratios in the weathering profiles contrast with those of Ca/Al, and Mg/Al ratios (Fig. 2), implying that the dissolution, mobility, and precipitation of Li differ from that of Mg and Ca. A measure of mobility of Li relative to Ca and Mg in the weathering profiles can be quantitatively understood from the following relative mobility parameter:

$$\left(\frac{\text{Li}}{\text{X}}\right)_{\text{RM}} = \frac{\left(\frac{\text{Li}}{\text{X}}\right)_{\text{profile}}}{\left(\frac{\text{Li}}{\text{X}}\right)_{\text{parent}}} \tag{13}$$

where X stands for Ca or Mg, and RM for relative mobility. A $\left(\frac{\text{Li}}{\text{X}}\right)_{\text{RM}}$ value of 1 indicates mobility of Li identical to that of Ca or Mg during weathering, whereas a value of less than 1 results from preferential release of Li over Ca or Mg. Substantial incorporation and scavenging of Li by secondary minerals would inhibit Li mobility, thus resulting in $\left(\frac{\text{Li}}{\text{X}}\right)_{\text{RM}} > 1$.

In the studied profiles, $\left(\frac{\text{Li}}{\text{Ca}}\right)_{\text{RM}}$ and $\left(\frac{\text{Li}}{\text{Mg}}\right)_{\text{RM}}$ values are in the range of 5.62–11.79 and 3.99–10.64, respectively (Table 2), suggesting decreased relative mobility of Li. In both studied profiles, the observed positive correlations of CIA with $\left(\frac{\text{Li}}{\text{Ca}}\right)_{\text{RM}}$ and $\left(\frac{\text{Li}}{\text{Mg}}\right)_{\text{RM}}$ (Fig. 8) suggest that as weathering intensity increases, higher abundances of clay minerals result in greater removal of Li from solution and thereby reducing its mobility relative to Ca and Mg. This interpretation is supported by the observed positive correlation of $\left(\frac{\text{Li}}{\text{Ca}}\right)_{\text{RM}}$ and $\left(\frac{\text{Li}}{\text{Mg}}\right)_{\text{RM}}$ with clay-sized fractions (Fig. S7).

As expected, significant inverse correlations are observed for $\delta^7 \text{Li}$ with both $\left(\frac{\text{Li}}{\text{Ca}}\right)_{\text{RM}}$ and $\left(\frac{\text{Li}}{\text{Mg}}\right)_{\text{RM}}$ (Fig. 8), indicating lower $\delta^7 \text{Li}$ values with increasing removal of Li from the solution. At incipient weathering, the release of Li, Ca and Mg appear to be less incongruent, as evident from $\left(\frac{\text{Li}}{\text{Ca}}\right)_{\text{RM}}$ and $\left(\frac{\text{Li}}{\text{Mg}}\right)_{\text{RM}}$ values closer to 1, possibly because of lower abundance of secondary minerals and decreased scavenging of Li from the fluids, leading to higher $\delta^7 \text{Li}$ values in the saprolites.

We also determined the relative mobility parameters and δ^7 Li values for each of the complete profiles using mass balance approach (See section S5). Based on the weathering profile data for the depth

intervals studied (Fig. 8), the empirical relationships of $\delta^7 \text{Li}$ with $\left(\frac{\text{Li}}{\text{Ca}}\right)_{\text{RM}}$, $\left(\frac{\text{Li}}{\text{Mg}}\right)_{\text{RM}}$ and CIA, and of $\left(\frac{\text{Li}}{\text{Ca}}\right)_{\text{RM}}$ and $\left(\frac{\text{Li}}{\text{Mg}}\right)_{\text{RM}}$ with CIA (Fig. 8 and Fig. S3a) were derived from regression of the data (Table S4). We demonstrate that δ^7 Li of the whole weathering profiles (See eq. 11), obtained from mass balance calculations are consistent, within the errors of estimations, with those obtained from the empirical relationships based on regression analyses of $\delta^7 \text{Li} - \left(\frac{\text{Li}}{\text{Ca}}\right)_{\text{RM}}$, $\delta^7 \text{Li} - \left(\frac{\text{Li}}{\text{Mg}}\right)_{\text{RM}}$, $\delta^7 \text{Li} - \text{CIA}$, $\left(\frac{\text{Li}}{\text{Ca}}\right)_{\text{RM}}$ - CIA and $\left(\frac{\text{Li}}{\text{Mg}}\right)_{\text{RM}}$ - CIA data (See Table S4). Therefore, this exercise shows that $\delta^7 \text{Li}$ values and relative mobility parameters $\left(\frac{\text{Li}}{\text{Ca}}\right)_{\text{RM}}$ and $\left(\frac{\text{Li}}{\text{Mg}}\right)_{\text{RM}}$ can be predicted using the CIA values of weathered materials, at least for basaltic weathering in the RVP.

Published data allow us to evaluate the relative mobilities of Li, Ca and Mg in weathering profiles developed on basaltic rocks under diverse climatic regimes and spanning a wide range of weathering intensities (Kisakurek et al., 2004; Li et al., 2020; Tong et al., 2021; Xiong et al., 2022). Our compilation indicates that $\left(\frac{\text{Li}}{\text{Ca}}\right)_{\text{RM}}$ and $\left(\frac{\text{Li}}{\text{Mg}}\right)_{\text{RM}}$ values vary by three to four orders of magnitude (Fig. S8). While weak to moderate inverse correlations are observed in the Bidar and Zhanjiang profile data, the trends differ notably for weathered basalts from the Hawaii and Hainan Islands. The data for the Hawaiian samples do not exhibit inverse correlations in $\delta^7 \text{Li-} \left(\frac{\text{Li}}{\text{Ca}}\right)_{\text{RM}}$ space, with significant differences observed between weathering under dry and humid conditions. This is mainly due to higher $\left(\frac{\text{Li}}{\text{Ca}}\right)_{\text{RM}}$ values observed in weathered basalts in humid conditions. In the Hainan islands, the $\delta^7 \text{Li}$ values of highly weathered basalts do not exhibit well defined covariation trends with either $\left(\frac{\text{Li}}{\text{Ca}}\right)_{\text{RM}}$ When the relative mobility parameters are plotted against CIA (Fig. S9), strong positive correlations are observed as expected, except for highly weathered basalts. At high weathering intensities (CIA>90), the relative mobility parameters

show significant higher variability within a narrow range of CIA values. Therefore, in the plots of $\delta^7 \text{Li}$ vs. $\left(\frac{\text{Li}}{\text{Ca}}\right)_{\text{RM}}$ and $\delta^7 \text{Li}$ vs. $\left(\frac{\text{Li}}{\text{Mg}}\right)_{\text{RM}}$, highly weathered samples exhibit steeper variation trends compared to moderately weathered samples. Hawaiian basalts weathered under humid conditions exhibit higher $\left(\frac{\text{Li}}{\text{Ca}}\right)_{\text{RM}}$ values, which form a cluster when plotted against CIA. Therefore, our compilation of global data on weathered basalts does not demonstrate consistent covariation between $\delta^7 \text{Li}$ and relative mobility parameters. This observation highlights the need for further studies to develop better understanding of processes regulating the relative mobilities of Li, Ca and Mg, particularly under conditions of intense chemical weathering.

We now assess if the δ^7 Li-CIA variation trends observed in this study also apply to the riverine suspended particulate matter (SPM). This exercise aims at evaluating whether δ^7 Li can be reliably predicted from the empirical δ^7 Li-CIA relationship. Our compilation of global riverine SPM data demonstrates significant positive covariation trends (Fig. 9), with a few outliers. Notably, the data from two profiles of this study align well the general variation trends observed in the riverine SPM dataset, although, as expected, the SPM data exhibit more scatter. Considering that the major element compositions and δ^7 Li of the riverine SPM are subject to significant solute-particle interactions, grain size variations and mineralogy during fluvial transport (Dellinger et al., 2014; Ma et al., 2020; Tipper et al., 2021), the general δ^7 Li-CIA correlation trend observed for the riverine SPM and weathered basalts is particularly striking. Based on this correlation, we propose that δ^7 Li values can be predicted from CIA values within the range of $\pm 0.01\%$ to $\pm 3.45\%$, with prediction accuracy improving at higher CIA values. Existing studies, however, are insufficient to assess whether this approach can be reliably extended to riverine sediments across space and time. Nonetheless, our observations and compilation of global data provide a useful framework for estimating δ^7 Li values of sediments directly from CIA values. We

acknowledge that such an empirical approach is simplistic and may be refined through future research. To establish δ^7 Li as an effective tracer of silicate weathering, a more comprehensive understanding of Li behaviour during fluid-particle interactions is required through further Li isotopic studies on weathering profiles, river waters and sediments. Such investigations are essential to gain insights into Li mobility relative to other cations and its influence on δ^7 Li signatures in both modern and ancient records.

6. Conclusions

In this study, we investigated two well-characterized basaltic weathering profiles in the Rajmahal Volcanic Province. Our interpretation framework combined findings from this study, outputs from mass balance and isotope fractionation models and global datasets from weathering profiles and river sediments in basaltic catchments. The findings and assessments of this study highlight following key features:

- i. Adsorption of Li onto secondary minerals of weathered basalts, accounting for a minor fraction of total Li, results in a preferential uptake of ⁶Li.
- ii. However, Li incorporation into clay-structures consistent with a batch fractionation model –
 dominates the total Li budget of the weathered basalts. The combined processes of adsorption,
 desorption and structural incorporation of Li govern the depth-dependent variation in δ⁷Li within
 the weathering profiles.
- 573 iii. The estimates of δ^7 Li of weathering solutions show excellent agreement between two independent approaches.
- **iv.** The empirical relations between $\delta^7 \text{Li}$, relative mobility indices $\left(\frac{\text{Li}}{\text{Ca}}\right)_{\text{RM}}$ and $\left(\frac{\text{Li}}{\text{Mg}}\right)_{\text{RM}}$ and CIA, in weathering profiles can be used to reliably predict the $\delta^7 \text{Li}$ and relative mobility indices for the entire weathering profiles.

578	V.	We demonstrate for the first time that δ' Li of riverine sediments can be predicted from CIA values
579		This framework would significantly advance efforts to establish $\delta^7 Li$ as a robust tracer of silicate
580		weathering intensity and relative mobilities of Li, Ca and Mg in both modern and ancient records
581		
582		
583		
584		
585		
586		
587		
588		
589		
590		
591		
592		
593		
594		
595		
596		
597		
598		
599		
600		
601		
602		

CRediT authorship contribution statement

- 605 Anup Kumar Sharma: Conceptualization, Investigation, Writing Original Draft, Project
- administration, Methodology, Validation, Formal analysis. Tarun Kumar Dalai: Conceptualization,
- 607 Investigation, Writing Original Draft, Writing Review & Editing, Resources, Supervision, Project
- administration, Funding acquisition, Methodology, Validation, Formal analysis. Sambuddha Misra:
- 609 Investigation, Writing Review & Editing, Resources, Methodology, Validation, Data Curation, Formal
- analysis. Prem Chand Kisku: Resources, Data Curation, Validation, Formal analysis. Jitendra Kumar
- 611 **Pattanaik:** Resources, Data Curation, Validation, Formal analysis.

612

613

604

Acknowledgements

- AKS thanks the Indian Council of Scientific and Industrial Research (CSIR), New Delhi for providing
- research fellowship (Award no.: 09/921(0229)2019-EMR-I). TKD acknowledges the financial support
- 616 through the ARF grant from IISER Kolkata. JKP acknowledges the SERB grant (SR/FTP/ES-158/2014).
- Mr. Haldhar Kumar is acknowledged for his assistance during fieldwork. We thank Dr. Santosh Ch. Das
- and Biswajit Giri for their assistance with analysis.

619

620

Appendix A. Supplementary Material

- 621 Supplementary material includes the following:
- 622 **Section S1.** Processing of samples
- 623 **Section S2:** Previously published data
- **Section S3:** Estimation of crystal-bound Li concentration in neo-formed clay minerals
- 625 **Section S4:** Calculation of δ^7 Li_{crystal-bound}
- **Section S5:** Calculation of CIA and mobility of Li relative to Ca and Mg for whole profiles
- **Figures:** Fig. S1 to Fig. S10.
- **Tables:** Table S1 to Table S4.

630

629

631

632

633

634

635

References

637

664 665

- Amiotte Suchet, P., Probst, J. L., Ludwig, W., 2003. Worldwide distribution of continental rock lithology:

 Implications for the atmospheric/soil CO2 uptake by continental weathering and alkalinity river transport to the oceans. Global biogeochemical cycles, 17(2).

 https://doi.org/10.1029/2002GB001891
- Baksi, A. K., 2022. Geochemistry and geochronology of the Rajmahal Flood Basalt Province, northeastern
 India: Genetic links to Kerguelen hotspot activity. *Journal of Earth System Science*, 131, 157.
 https://doi.org/10.1007/s12040-022-01855-8
- Bardossy, G. Y., 1981. Paleoenvironments of laterites and lateritic bauxites—Effect of global tectonism and bauxite formation. In: Banerjee P K (ed) Proceedings of the international Seminar on lateritisation processes, Trivandum, Geolog Survey India, pp 287–294.
- Bohlin, M. S., Misra, S., Lloyd, N., Elderfield, H., Bickle, M. J., 2018. High-precision determination of lithium and magnesium isotopes utilising single column separation and multi-collector inductively coupled plasma mass spectrometry. Rapid Communications in Mass Spectrometry, 32(2), 93-104. https://doi.org/10.1002/rcm.8020
- Bouchez, J., Gaillardet, J., France-Lanord, C., Maurice, L., Dutra-Maia, P., 2011. Grain size control of river suspended sediment geochemistry: Clues from Amazon River depth profiles. Geochemistry, Geophysics, Geosystems, 12(3). https://doi.org/10.1029/2010GC003380
- Bouchez, J., von Blanckenburg, F., 2021. The role of vegetation in setting strontium stable isotope ratios in the Critical Zone. American Journal of Science, 321(8), 1246-1283. https://doi.org/10.2475/08.2021.04
- Bouchez, J., Von Blanckenburg, F., Schuessler, J. A., 2013. Modeling novel stable isotope ratios in the weathering zone. American Journal of Science, 313(4), 267-308. https://doi.org/10.2475/04.2013.01
- Cai, D., Henehan, M. J., Uhlig, D., von Blanckenburg, F., 2024. Lithium isotopes in water and regolith in
 a deep weathering profile reveal imbalances in Critical Zone fluxes. Geochimica et Cosmochimica
 Acta, 369, 213-226. https://doi.org/10.1016/j.gca.2024.01.012
 - Chan, L. H., Edmond, J. M., Thompson, G., Gillis, K., 1992. Lithium isotopic composition of submarine basalts: implications for the lithium cycle in the oceans. Earth and Planetary Science Letters, 108(1-3), 151-160. https://doi.org/10.1016/0012-821X(92)90067-6
- Chan, L. H., Hein, J. R., 2007. Lithium contents and isotopic compositions of ferromanganese deposits
 from the global ocean. Deep Sea Research Part II: Topical Studies in Oceanography, 54(11-13),
 1147-1162. https://doi.org/10.1016/j.dsr2.2007.04.003
- Chapela Lara, M., Buss, H. L., Henehan, M. J., Schuessler, J. A., McDowell, W. H., 2022. Secondary minerals drive extreme lithium isotope fractionation during tropical weathering. Journal of Geophysical Research: Earth Surface, 127(2), e2021JF006366.

 https://doi.org/10.1029/2021JF006366
- Chetelat, B., Liu, C. Q., Gaillardet, J., Wang, Q. L., Zhao, Z. Q., Liang, C. S., Xiao, Y. K., 2009. Boron isotopes geochemistry of the Changjiang basin rivers. Geochimica et Cosmochimica Acta, 73(20), 6084-6097. https://doi.org/10.1016/j.gca.2009.07.026

- Clergue, C., Dellinger, M., Buss, H. L., Gaillardet, J., Benedetti, M. F., Dessert, C., 2015. Influence of atmospheric deposits and secondary minerals on Li isotopes budget in a highly weathered catchment, Guadeloupe (Lesser Antilles). Chemical Geology, 414, 28-41. https://doi.org/10.1016/j.chemgeo.2015.08.015
- 681 Dellinger, M., Gaillardet, J., Bouchez, J., Calmels, D., Galy, V., Hilton, R.G., Louvat, P., France-Lanord, 682 C., 2014. Lithium isotopes in large rivers reveal the cannibalistic nature of modern continental Letters, weathering and erosion. Earth and Planetary Science 401. 683 359-372. https://doi.org/10.1016/j.epsl.2014.05.061 684
- Dellinger, M., Gaillardet, J., Bouchez, J., Calmels, D., Louvat, P., Dosseto, A., Gorge, C., Alanoca, L.,
 Maurice, L., 2015. Riverine Li isotope fractionation in the Amazon River basin controlled by the
 weathering regimes. Geochimica et Cosmochimica Acta 164, 71-93.

 https://doi.org/10.1016/j.gca.2015.04.042
- Delvigne, C., Opfergelt, S., Cardinal, D., Hofmann, A., André, L., 2016. Desilication in Archean weathering processes traced by silicon isotopes and Ge/Si ratios. Chemical Geology, 420, 139-147. https://doi.org/10.1016/j.chemgeo.2015.11.007
- Dessert, C., Dupre, B., Gaillardet, J., François, L. M., Allegre, C. J., 2003. Basalt weathering laws and the impact of basalt weathering on the global carbon cycle. Chemical Geology 202, 257-273. https://doi.org/10.1016/j.chemgeo.2002.10.001
- Eylem, C., Erten, H. N., & Göktürk, H. (1990). Sorption-desorption behaviour of barium on clays. Journal of environmental radioactivity, 11(2), 183-200. https://doi.org/10.1016/0265-931X(90)90061-Y
- Frings, P., Oelze, M., Schubring, F., Frick, D. A., von Blanckenburg, F., 2021. Interpreting silicon isotopes in the critical zone. American Journal of Science, 321(8), 1164-1203. https://doi.org/10.2475/08.2021.02
- Gaillardet, J. D. B. L., Dupré, B., Louvat, P., Allegre, C. J., 1999. Global silicate weathering and CO2 consumption rates deduced from the chemistry of large rivers. Chemical geology, 159(1-4), 3-30. https://doi.org/10.1016/S0009-2541(99)00031-5
- Gaillardet, J., Dupre, B., Allegre, C. J., Négrel, P., 1997. Chemical and physical denudation in the Amazon River Basin. Chemical geology, 142(3-4), 141-173. https://doi.org/10.1016/S0009-2541(97)00074-0
- Hoyer, M., Kummer, N. A., Merkel, B., 2015. Sorption of lithium on bentonite, kaolin and zeolite. Geosciences, 5(2), 127-140. https://doi.org/10.3390/geosciences5020127
- 708 Ghose, N. C., Chatterjee, N., Windley, B. F., 2017. Subaqueous Eruptive Phase of the Late Aaptian 709 Rajmahal Volcanism India: Evidence from Volcaniclastic Rocks, Bentonite, Black Shales and 710 Oolite. *Geoscience Frontiers*, 8, 809-822. https://doi.org/10.1016/j.gsf.2016.06.007
- Gou, L.F., Jin, Z., von Strandmann, P.A.P., Li, G., Qu, Y.X., Xiao, J., Deng, L., Galy, A., 2019. Li isotopes
 in the middle Yellow River: Seasonal variability, sources and fractionation. Geochimica et
 Cosmochimica Acta 248, 88-108. https://doi.org/10.1016/j.gca.2019.01.007
- Gupta S. K., Chen K. Y., 1975. Partitioning of trace metals in selective chemical fractions of near shore sediments. *Environmental Letters*, 10, 129. https://doi.org/10.1080/00139307509435816

- Hao, W., Mänd, K., Swaren, L., Myers, K.D., Lalonde, S., Wilmeth, D.T., Van Zuilen, M., Wilson, S.,
 Alessi, D.S., Konhauser, K.O., 2021. Trace elemental partitioning on clays derived from
 hydrothermal muds of the El Tatio Geyser Field, Chile. *Journal of Geophysical Research: Solid Earth*, 126(5), e2020JB021422. https://doi.org/10.1029/2020JB021422
- Hindshaw, R. S., Tosca, R., Gout, T. L., Farnan, I., Tosca, N. J., Tipper, E. T., 2019. Experimental constraints on Li isotope fractionation during clay formation. Geochimica et Cosmochimica Acta 250, 219-237. https://doi.org/10.1016/j.gca.2019.02.015
- Huh, Y., Chan, L. H., Chadwick, O. A., 2004. Behavior of lithium and its isotopes during weathering of
 Hawaiian basalt. Geochemistry, Geophysics, Geosystems, 5(9).
 https://doi.org/10.1029/2004GC000729
- Huh, Y., Chan, L. H., Edmond, J. M., 2001. Lithium isotopes as a probe of weathering processes: Orinoco River. Earth and Planetary Science Letters 194, 189-199. https://doi.org/10.1016/S0012-821X(01)00523-4
- Huh, Y., Chan, L. H., Zhang, L., Edmond, J. M., 1998. Lithium and its isotopes in major world rivers: implications for weathering and the oceanic budget. Geochimica et Cosmochimica Acta 62, 2039-2051. https://doi.org/10.1016/S0016-7037(98)00126-4
- Jin, L., Ravella, R., Ketchum, B., Bierman, P. R., Heaney, P., White, T., Brantley, S. L., 2010. Mineral weathering and elemental transport during hillslope evolution at the Susquehanna/Shale Hills Critical Zone Observatory. Geochimica et Cosmochimica Acta, 74(13), 3669-3691. https://doi.org/10.1016/j.gca.2010.03.036
- Juzer, S., Tanwar, N., Misra, S., 2022. Precise determination of lithium isotope ratios at the sub-nanogram level by QQQ-ICP-MS: application to natural waters and carbonates. Journal of Analytical Atomic Spectrometry, 37(7), 1541-1553. https://doi.org/10.1039/D2JA00069E
- Kabata-Pendias, A., Pendias, H., 2001. Trace metals in soils and plants. CRC Press, Boca Raton.
- Khalifa, A. Z., Cizer, Ö., Pontikes, Y., Heath, A., Patureau, P., Bernal, S. A., Marsh, A. T., 2020. Advances
 in alkali-activation of clay minerals. Cement and Concrete Research, 132, 106050.
 https://doi.org/10.1016/j.cemconres.2020.106050
- Kısakürek, B., Widdowson, M., James, R. H., 2004. Behaviour of Li isotopes during continental weathering: the Bidar laterite profile, India. Chemical Geology, 212(1-2), 27-44. https://doi.org/10.1016/j.chemgeo.2004.08.027
- Kurtz, A. C., Derry, L. A., Chadwick, O. A., 2001. Accretion of Asian dust to Hawaiian soils: isotopic, elemental, and mineral mass balances. Geochimica et Cosmochimica acta, 65, 1971-1983.
 https://doi.org/10.1016/S0016-7037(01)00575-0
- Lemarchand, E., Chabaux, F., Vigier, N., Millot, R., Pierret, M. C., 2010. Lithium isotope systematics in a forested granitic catchment (Strengbach, Vosges Mountains, France). Geochimica et Cosmochimica Acta 74, 4612-4628. https://doi.org/10.1016/j.gca.2010.04.057
- Li, W., Liu, X. M., 2020. Experimental investigation of lithium isotope fractionation during kaolinite adsorption: Implications for chemical weathering. Geochimica et Cosmochimica Acta 284, 156-172. https://doi.org/10.1016/j.gca.2020.06.025

- Li, W., Liu, X. M., 2020. Experimental investigation of lithium isotope fractionation during kaolinite adsorption: Implications for chemical weathering. Geochimica et Cosmochimica Acta, 284, 156-172. https://doi.org/10.1016/j.gca.2020.06.025
- Li, W., Liu, X. M., Chadwick, O. A., 2020. Lithium isotope behavior in Hawaiian regoliths: Soilatmosphere-biosphere exchanges. Geochimica et Cosmochimica Acta, 285, 175-192. https://doi.org/10.1016/j.gca.2020.07.012
- Liu, X. M., Rudnick, R. L., McDonough, W. F., Cummings, M. L., 2013. Influence of chemical weathering
 on the composition of the continental crust: Insights from Li and Nd isotopes in bauxite profiles
 developed on Columbia River Basalts. Geochimica et Cosmochimica Acta, 115, 73-91.
 https://doi.org/10.1016/j.gca.2013.03.043
- Liu, X. M., Wanner, C., Rudnick, R. L., McDonough, W. F., 2015. Processes controlling δ7Li in rivers
 illuminated by study of streams and groundwaters draining basalts. Earth and Planetary Science
 Letters, 409, 212-224. https://doi.org/10.1016/j.epsl.2014.10.032
- Lupker, M., France-Lanord, C., Galy, V., Lavé, J., Kudrass, H., 2013. Increasing chemical weathering in
 the Himalayan system since the Last Glacial Maximum. Earth and Planetary Science Letters, 365,
 243-252. https://doi.org/10.1016/j.epsl.2013.01.038
- Ma, J. L., Wei, G. J., Xu, Y. G., Long, W. G., Sun, W. D., 2007. Mobilization and re-distribution of major
 and trace elements during extreme weathering of basalt in Hainan Island, South China. Geochimica
 et Cosmochimica Acta 71, 3223-3237. https://doi.org/10.1016/j.gca.2007.03.035
- Ma, T., Weynell, M., Li, S.L., Liu, Y., Chetelat, B., Zhong, J., Xu, S., Liu, C.Q., 2020. Lithium isotope compositions of the Yangtze River headwaters: Weathering in high-relief catchments. Geochimica et Cosmochimica Acta, 280, 46-65. https://doi.org/10.1016/j.gca.2020.03.029
- Millot, R., Vigier, N., Gaillardet, J., 2010. Behaviour of lithium and its isotopes during weathering in the
 Mackenzie Basin, Canada. Geochimica et Cosmochimica Acta, 74(14), 3897-3912.
 https://doi.org/10.1016/j.gca.2010.04.025
- Misra, S., Froelich, P. N., 2012. Lithium isotope history of Cenozoic seawater: changes in silicate weathering and reverse weathering. science, 335(6070), 818-823. http://dx.doi.org/10.1126/science.1214697
- Mukherjee, P. K., 1971. Petrology of Rajmahal Traps of the NW Rajmahal Hills, India. *Bulletin of Volcanology*, *35*, 887-906. https://doi.org/10.1007/BF02596853
- Négrel, P., & Millot, R. (2019). Behaviour of Li isotopes during regolith formation on granite (Massif Central, France): Controls on the dissolved load in water, saprolite, soil and sediment. Chemical Geology, 523, 121-132. http://dx.doi.org/10.1016/j.chemgeo.2019.05.037
- Nesbitt, H. W., 1979. Mobility and fractionation of rare earth elements during weathering of a granodiorite. *Nature*, *279*, 206-210. https://doi.org/10.1038/279206a0
- Nesbitt, H. W., Markovics, G., Price, R. C., 1980. Chemical processes affecting alkalis and alkaline earths during continental weathering. Geochimica et Cosmochimica Acta 44, 1659-1666. https://doi.org/10.1016/0016-7037(80)90218-5
- Nesbitt, H. W., Young, G. M., 1982. Early Proterozoic climates and plate motions inferred from major element chemistry of lutites. *Nature*, *299*, 715-717. http://dx.doi.org/10.1038/299715a0

- Park, H., Singhal, N., Jho, E. H., 2015. Lithium sorption properties of HMnO in seawater and wastewater. *Water research* 87, 320-327. https://doi.org/10.1016/j.watres.2015.09.032
- Pistiner, J. S., Henderson, G. M., 2003. Lithium-isotope fractionation during continental weathering processes. Earth and Planetary Science Letters 214, 327-339. https://doi.org/10.1016/S0012-821X(03)00348-0
- Pogge von Strandmann, P. A. P., Burton, K. W., James, R. H., van Calsteren, P., Gíslason, S. R., 800 Mokadem, F., 2006. Riverine behaviour of uranium and lithium isotopes in an actively glaciated 801 basaltic terrain. Earth and Planetary Science Letters, 251(1-2), 802 134-147. 803 https://doi.org/10.1016/j.epsl.2006.09.001
- Pogge von Strandmann, P. A. P., Burton, K. W., James, R. H., van Calsteren, P., Gislason, S. R., 2010.
 Assessing the role of climate on uranium and lithium isotope behaviour in rivers draining a basaltic terrain. Chemical Geology, 270(1-4), 227-239. https://doi.org/10.1016/j.chemgeo.2009.12.002
- Pogge von Strandmann, P. A. P., Burton, K. W., Opfergelt, S., Eiríksdóttir, E. S., Murphy, M. J., Einarsson, A., Gislason, S. R., 2016. The effect of hydrothermal spring weathering processes and primary productivity on lithium isotopes: Lake Myvatn, Iceland. Chemical Geology 445, 4-13. https://doi.org/10.1016/j.chemgeo.2016.02.026
- Pogge von Strandmann, P. A. P., Fraser, W. T., Hammond, S. J., Tarbuck, G., Wood, I. G., Oelkers, E. H., Murphy, M. J., 2019. Experimental determination of Li isotope behaviour during basalt weathering. Chemical Geology, 517, 34-43. https://doi.org/10.1016/j.chemgeo.2019.04.020
- Pogge von Strandmann, P. A. P., Frings, P. J., Murphy, M. J., 2017b. Lithium isotope behaviour during weathering in the Ganges Alluvial Plain. Geochimica et Cosmochimica Acta, 198, 17-31. https://doi.org/10.1016/j.gca.2016.11.017
- Pogge von Strandmann, P. A. P., Kasemann, S. A., Wimpenny, J. B., 2020. Lithium and lithium isotopes in Earth's surface cycles. Elements: An International Magazine of Mineralogy, Geochemistry, and Petrology, 16(4), 253-258. https://doi.org/10.2138/gselements.16.4.253
- Pogge von Strandmann, P. A. P., Opfergelt, S., Lai, Y. J., Sigfusson, B., Gislason, S. R., Burton, K. W., 2012. Lithium, magnesium and silicon isotope behaviour accompanying weathering in a basaltic soil and pore water profile in Iceland. Earth and Planetary Science Letters, 339, 11-23. https://doi.org/10.1016/j.epsl.2012.05.035
- Pogge von Strandmann, P. A. P., Vaks, A., Bar-Matthews, M., Ayalon, A., Jacob, E., Henderson, G. M., 824 825 2017a. Lithium isotopes in speleothems: Temperature-controlled variation in silicate weathering 826 during glacial cycles. Earth and Planetary Science Letters, 469, 64-74. https://doi.org/10.1016/j.epsl.2017.04.014 827
- Pogge von Strandmann, P. A., Henderson, G. M., 2015. The Li isotope response to mountain uplift. Geology 43, 67-70. http://dx.doi.org/10.1130/G36162.1
- Pogge von Strandmann, P.A.P., Cosford, L.R., Liu, C.Y., Liu, X., Krause, A.J., Wilson, D.J., He, X., McCoy-West, A.J., Gislason, S.R. and Burton, K.W., 2023. Assessing hydrological controls on the lithium isotope weathering tracer. Chemical Geology, 642, 121801.
- https://doi.org/10.1016/j.chemgeo.2023.121801

- Prodromou, K. P., 2016. Lithium adsorption on amorphous aluminum hydroxides and gibbsite. *Eurasian Journal of Soil Science 5*, 13-16. http://dx.doi.org/10.18393/ejss.2016.1.013-016
- Pryor, E. J., Tangunan, D., van der Lubbe, H. J. L., Simon, M. H., Hall, I. R., 2024. Recommended centrifuge method: Specific grain size separation in the< 63 μm fraction of marine sediments.
 MethodsX 12, 102718. https://doi.org/10.1016/j.mex.2024.102718
- Rad, S. D., Allegre, C. J., Louvat, P., 2007. Hidden erosion on volcanic islands. Earth and Planetary Science Letters 262, 109-124. http://dx.doi.org/10.1016/j.epsl.2007.07.019
- Raymo, M. E., Ruddiman, W. F., Froelich, P. N., 1988. Influence of late Cenozoic Mountain building on ocean geochemical cycles. Geology, 16(7), 649-653. https://doi.org/10.1130/0091-7613(1988)016%3C0649:IOLCMB%3E2.3.CO;2
- Raymo, M.E., Ruddiman, W.F., 1992. Tectonic forcing of late Cenozoic climate. Nature 359, 117–122.
 https://doi.org/10.1038/359117a0
- Rudnick, R. L., Tomascak, P. B., Njo, H. B., Gardner, L. R., 2004. Extreme lithium isotopic fractionation during continental weathering revealed in saprolites from South Carolina. Chemical Geology 212, 45-57. https://doi.org/10.1016/j.chemgeo.2004.08.008
- Ryu, J. S., Vigier, N., Lee, S. W., Lee, K. S., Chadwick, O. A., 2014. Variation of lithium isotope geochemistry during basalt weathering and secondary mineral transformations in Hawaii.
 Geochimica et Cosmochimica Acta, 145, 103-115. https://doi.org/10.1016/j.gca.2014.08.030
- Sajih, M., Bryan, N.D., Livens, F.R., Vaughan, D.J., Descostes, M., Phrommavanh, V., Nos, J., Morris,
 K., 2014. Adsorption of radium and barium on goethite and ferrihydrite: A kinetic and surface
 complexation modelling study. Geochimica et Cosmochimica Acta, 146, 150-163.
 https://doi.org/10.1016/j.gca.2014.10.008
- Sauzéat, L., Rudnick, R. L., Chauvel, C., Garçon, M., Tang, M., 2015. New perspectives on the Li isotopic composition of the upper continental crust and its weathering signature. Earth and Planetary Science Letters, 428, 181-192. https://doi.org/10.1016/j.epsl.2015.07.032
- Sharma, A. K., Dalai, T. K., Kisku, P. C., Pattanaik, J. K., Misra, S., Verma, S., Shukla, A. D., 2025.

 Release and partitioning of neodymium and its radiogenic isotope during basaltic weathering.

 Chemical Geology, 122957. https://doi.org/10.1016/j.chemgeo.2025.122957
- Taylor, S.R., McLennan, S.M., 1985. The Continental Crust: Its Composition and Evolution. Blackwell, Oxford, UK, 349.
- Teng, F. Z., Li, W. Y., Rudnick, R. L., Gardner, L. R., 2010. Contrasting lithium and magnesium isotope fractionation during continental weathering. Earth and Planetary Science Letters, 300(1-2), 63-71. https://doi.org/10.1016/j.epsl.2010.09.036
- Tipper, E. T., Calmels, D., Gaillardet, J., Louvat, P., Capmas, F., Dubacq, B., 2012. Positive correlation between Li and Mg isotope ratios in the river waters of the Mackenzie Basin challenges the interpretation of apparent isotopic fractionation during weathering. Earth and Planetary Science Letters, 333, 35-45. https://doi.org/10.1016/j.epsl.2012.04.023
- Tipper, E.T., Stevenson, E.I., Alcock, V., Knight, A.C., Baronas, J.J., Hilton, R.G., Bickle, M.J., Larkin, C.S., Feng, L., Relph, K.E., Hughes, G., 2021. Global silicate weathering flux overestimated

- because of sediment–water cation exchange. Proceedings of the National Academy of Sciences, 118(1), e2016430118. https://doi.org/10.1073/pnas.2016430118
- Tong, F., Xiao, Y., Sun, H., Wang, Y., Wan, H., Gou, L.F., Gong, Y., Huang, F., Li, D.Y., Hou, Z., 2021.
 Lithium isotopic features of Quaternary basaltic saprolite, Zhanjiang, China: Atmospheric input and clay-mineral adsorption. Science of The Total Environment, 785, 147235.
 https://doi.org/10.1016/j.scitotenv.2021.147235
- Vigier, N., Decarreau, A., Millot, R., Carignan, J., Petit, S., France-Lanord, C., 2008. Quantifying Li isotope fractionation during smectite formation and implications for the Li cycle. Geochimica et Cosmochimica Acta 72, 780-792. https://doi.org/10.1016/j.gca.2007.11.011
- Vigier, N., Decarreau, A., Millot, R., Carignan, J., Petit, S., France-Lanord, C., 2008. Quantifying Li isotope fractionation during smectite formation and implications for the Li cycle. Geochimica et Cosmochimica Acta, 72(3), 780-792. https://doi.org/10.1016/j.gca.2007.11.011
- Walker, J. C., Hays, P. B., Kasting, J. F., 1981. A negative feedback mechanism for the long-term stabilization of Earth's surface temperature. Journal of Geophysical Research: Oceans, 86(C10), 9776-9782. http://dx.doi.org/10.1029/JC086iC10p09776
- Wang, Q.L., Chetelat, B., Zhao, Z.Q., Ding, H., Li, S.L., Wang, B.L., Li, J. and Liu, X.L., 2015. Behavior of lithium isotopes in the Changjiang River system: Sources effects and response to weathering and erosion. Geochimica et Cosmochimica Acta, 151, 117-132.
 https://doi.org/10.1016/j.gca.2014.12.015
- Williams, L. B., Hervig, R. L., 2005. Lithium and boron isotopes in illite-smectite: The importance of crystal size. Geochimica et Cosmochimica Acta, 69(24), 5705-5716. https://doi.org/10.1016/j.gca.2005.08.005
- Wimpenny, J., Colla, C. A., Yu, P., Yin, Q. Z., Rustad, J. R., Casey, W. H., 2015. Lithium isotope fractionation during uptake by gibbsite. Geochimica et Cosmochimica Acta, 168, 133-150. https://doi.org/10.1016/j.gca.2015.07.011
 - Wimpenny, J., Gíslason, S. R., James, R. H., Gannoun, A., Von Strandmann, P. A. P., Burton, K. W., 2010a. The behaviour of Li and Mg isotopes during primary phase dissolution and secondary mineral formation in basalt. Geochimica et Cosmochimica Acta 74, 5259-5279. https://doi.org/10.1016/j.gca.2010.06.028

898

899

900

901

902 903

904

- Wimpenny, J., James, R. H., Burton, K. W., Gannoun, A., Mokadem, F., Gíslason, S. R., 2010b. Glacial effects on weathering processes: New insights from the elemental and lithium isotopic composition of West Greenland rivers. Earth and Planetary Science Letters, 290(3-4), 427-437. https://doi.org/10.1016/j.epsl.2009.12.042
- Xiong, Y. W., Qi, H. W., Hu, R. Z., Xiao, Y. L., Wei, L. Y., 2022. Lithium isotope behavior under extreme
 tropical weathering: A case study of basalts from the Hainan Island, South China. Applied
 Geochemistry, 140, 105295. https://doi.org/10.1016/j.apgeochem.2022.105295
- Yamaji, K., Makita, Y., Watanabe, H., Sonoda, A., Kanoh, H., Hirotsu, T., Ooi, K., 2001. Theoretical
 estimation of lithium isotopic reduced partition function ratio for lithium ions in aqueous solution.
 The Journal of Physical Chemistry A, 105(3), 602-613. https://doi.org/10.1021/jp001303i

- Zhang, J.W., Zhao, Z.Q., Yan, Y.N., Cui, L.F., Wang, Q.L., Meng, J.L., Li, X.D., Liu, C.Q., 2021. Lithium
 and its isotopes behavior during incipient weathering of granite in the eastern Tibetan Plateau,
 China. Chemical Geology, 559, 119969. https://doi.org/10.1016/j.chemgeo.2020.119969
- Zhang, P. C., Brady, P. V., Arthur, S. E., Zhou, W. Q., Sawyer, D., Hesterberg, D. A., 2001. Adsorption of barium (II) on montmorillonite: an EXAFS study. Colloids and Surfaces A: Physicochemical and Engineering Aspects, 190(3), 239-249. https://doi.org/10.1016/S0927-7757(01)00592-1
- Rozalen, M., Huertas, F. J., Brady, P. V., 2009. Experimental study of the effect of pH and temperature on the kinetics of montmorillonite dissolution. Geochimica et Cosmochimica Acta, 73(13), 3752-3766. https://doi.org/10.1016/j.gca.2009.03.026
- Zhu, G., Ma, J., Wei, G., Zhang, L., Wang, Z., Zhang, Z., Zeng, T., 2023. Lithium isotope fractionation during the weathering of granite: Responses to pH. Geochimica et Cosmochimica Acta 345, 117-129. https://doi.org/10.1016/j.gca.2022.12.028
- Zhu, Z. Y., Yang, T., Zhu, X. K., 2019. Achieving rapid analysis of Li isotopes in high-matrix and low Li samples with MC-ICP-MS: New developments in sample preparation and mass bias behavior
 of Li in ICPMS. Journal of Analytical Atomic Spectrometry, 34(7), 1503-1513.
 https://doi.org/10.1039/C9JA00076C

928 Figures

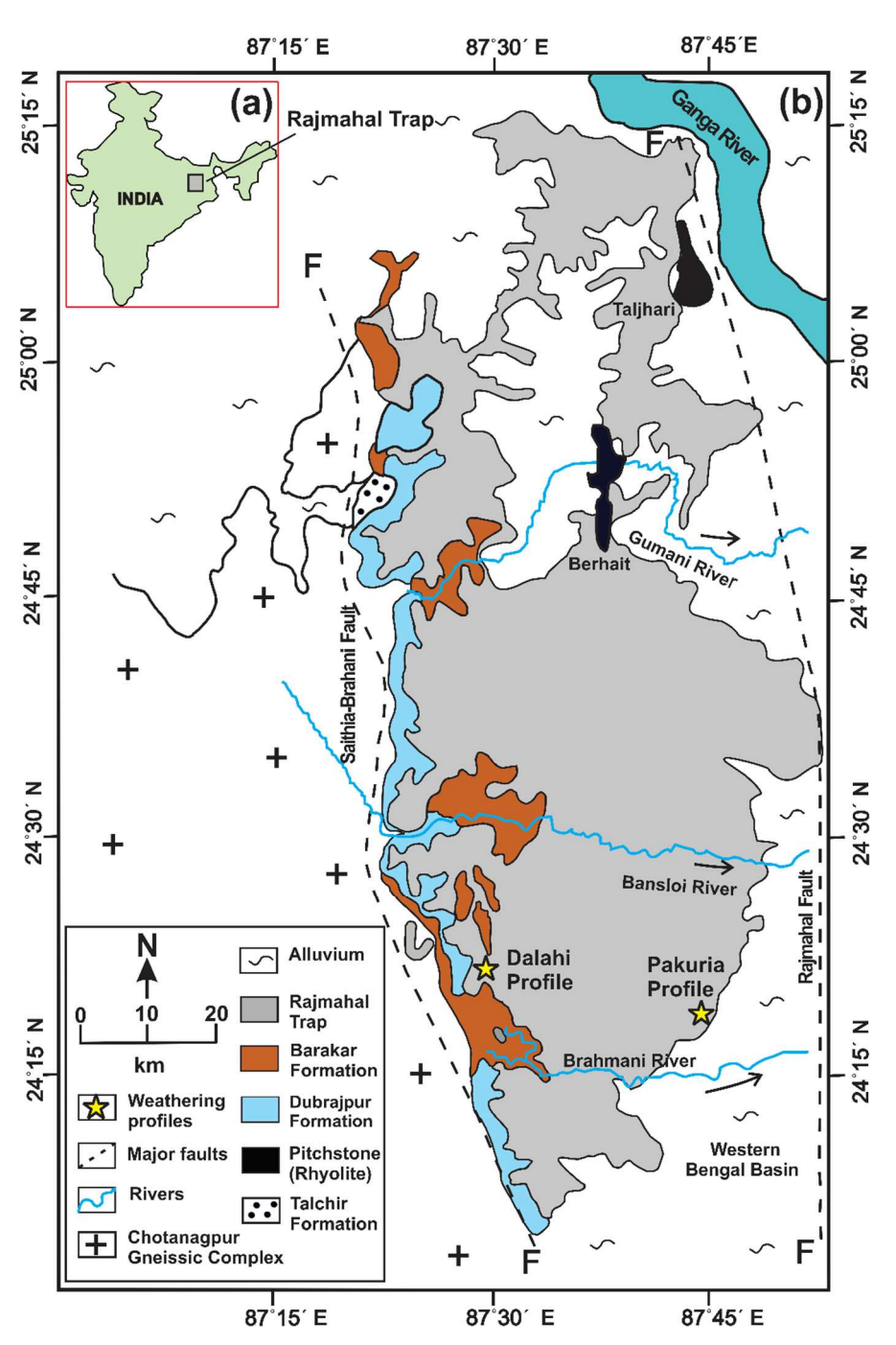


Fig. 1. The Rajmahal Volcanic Province (RVP) and the study area. **(a)** The areal extent of the trap basalts of the RVP in India. **(b)** Geological map of the RVP (modified after Ghose et al., 2017), showing the distribution of trap basalts and the locations of the studied weathering profiles (red stars). The map also shows the Gondwana Supergroup formations (Dubrajpur, Barakar and Talchir) and Chotanagpur granite-gneiss terrain.

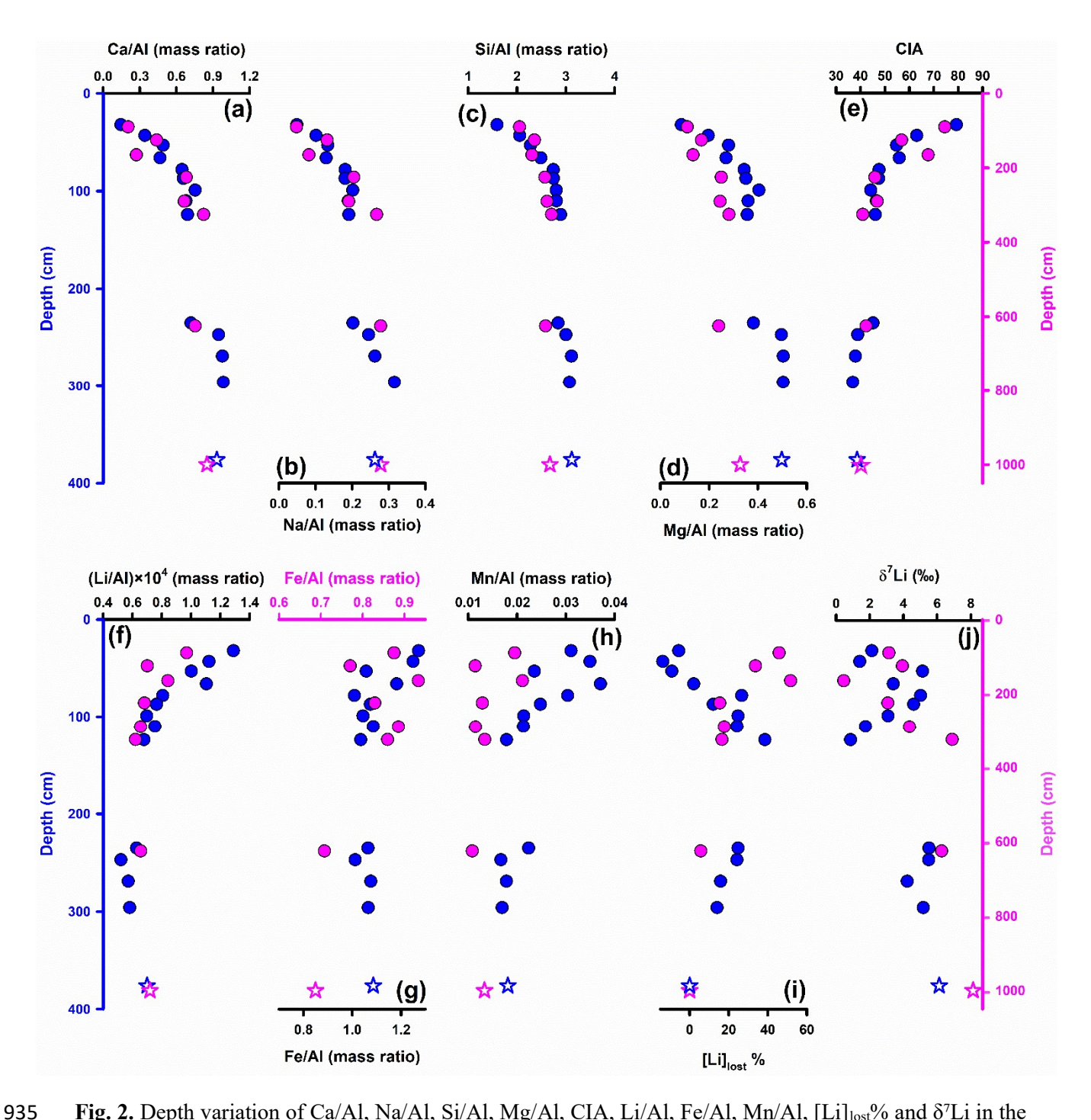


Fig. 2. Depth variation of Ca/Al, Na/Al, Si/Al, Mg/Al, CIA, Li/Al, Fe/Al, Mn/Al, [Li]_{lost}% and δ ⁷Li in the Dalahi (blue) and Pakuria profile (pink). Stars represent the parent basalt compositions. The upward decrease in the ratios of Ca/Al (a), Na/Al (b), Si/Al (c), and Mg/Al (d), combined with the upward increase in the CIA (e), suggest progressive loss of elements due to chemical weathering. The upward increasing variations in the Li/Al (f), Fe/Al (g) and Mn/Al (h) suggest enrichment of Li in the upper profiles is driven by sorption processes. The [Li]_{lost}% (i) increases upward with increase in CIA (e), except in the upper ~110 cm of the Dalahi profile, where [Li]_{lost}% shows a decreasing trend. Upward-decreasing trends of δ⁷Li (j) are evident in both the profiles except in the upper sections, where δ⁷Li values increase before decreasing (See discussion in subsection 5.2). Note different scales of Fe/Al ratio and depth for two profiles.

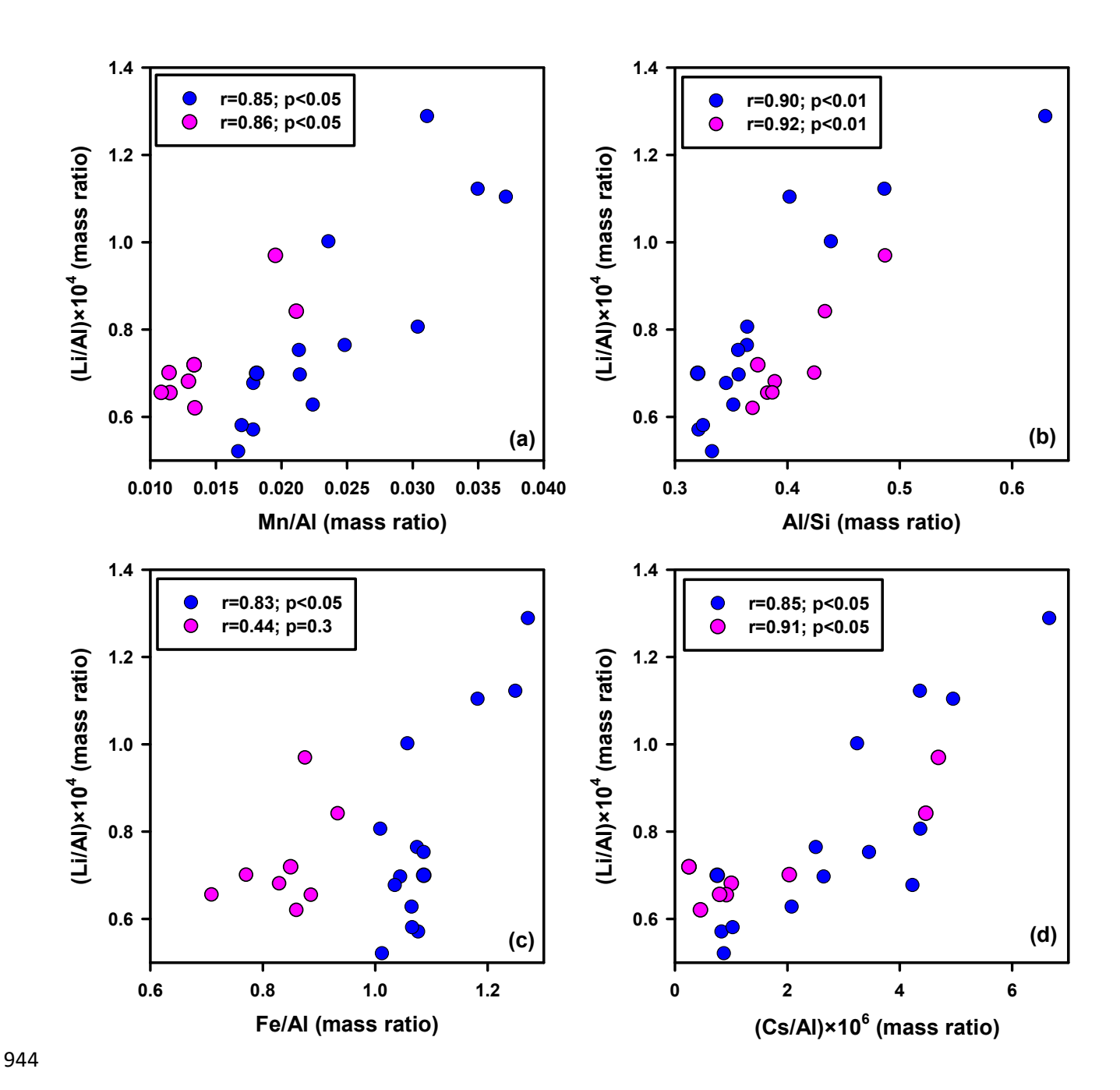


Fig. 3. Significant positive correlations are evident for Li/Al ratio with Mn/Al (a), Al/Si (b), Fe/Al (c) and Cs/Al (d) ratios, with the exception of a weak positive correlation between the Li/Al and Fe/Al in Pakuria Profile. These observations are suggestive of association of Li with clay minerals and oxyhydroxides. Dalahi profile (blue) and Pakuria profile (pink).

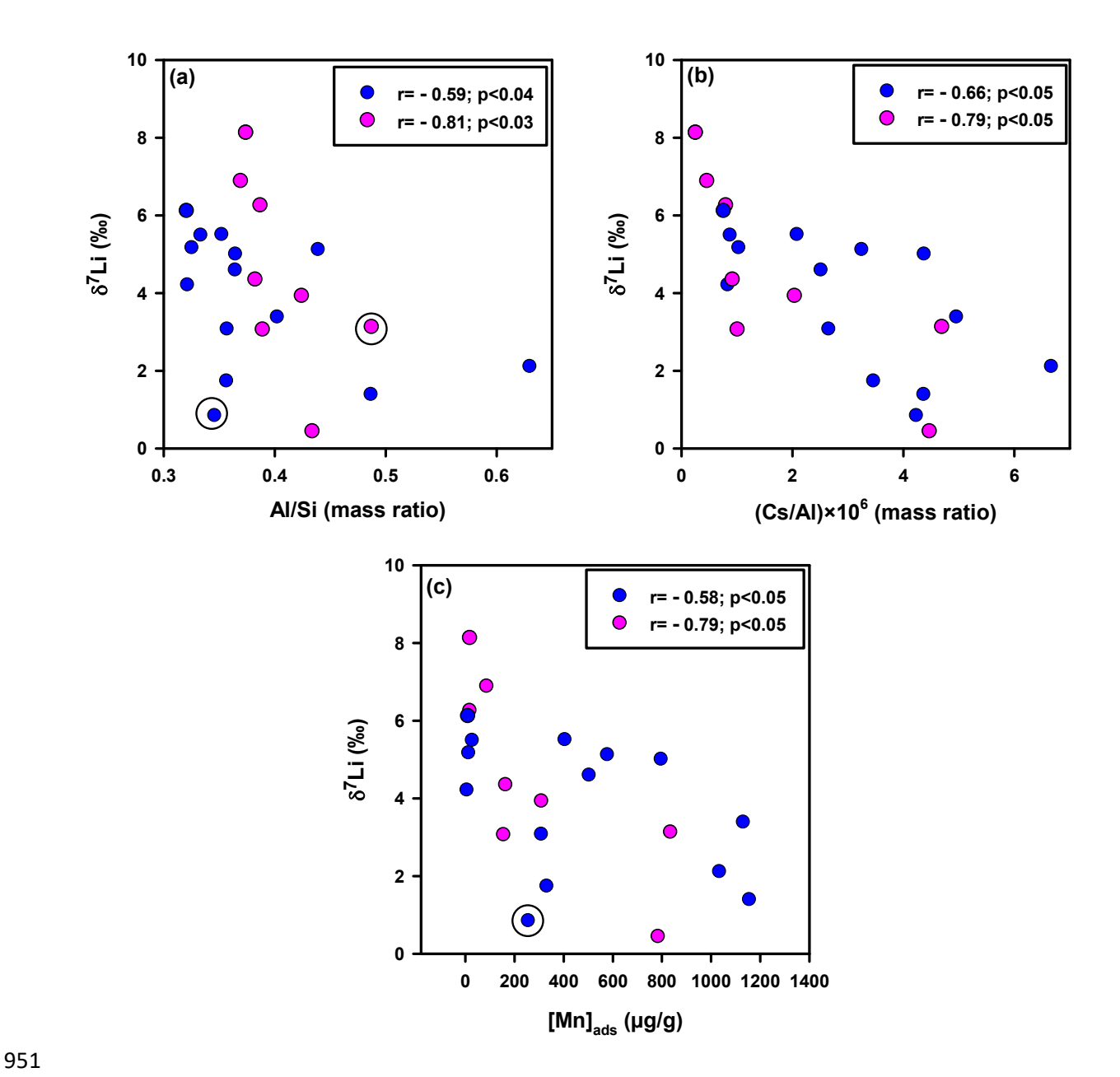


Fig. 4. The observed significant inverse correlation of δ^7 Li with Al/Si (a), Cs/Al (b) and [Mn]_{ads} (c), suggests that the sorption of Li (see Fig. 3) contributes to the lower δ^7 Li values in the profiles. The outliers (circled) are excluded from regression analysis. Dalahi profile (blue), Pakuria profile (pink).

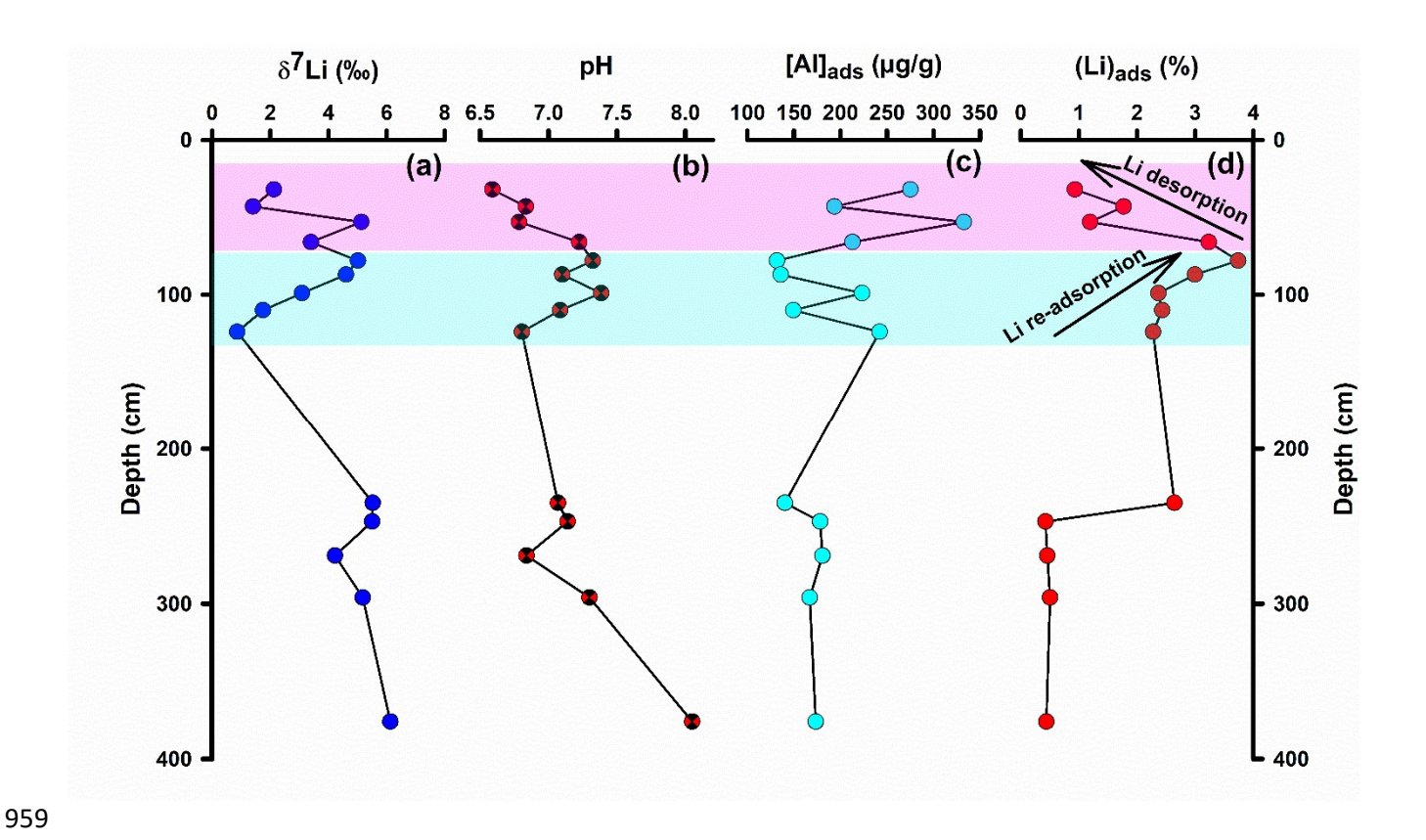


Fig. 5. Depth variation of δ^7 Li, pH, [Al]_{ads} and Li_{ads}% in the Dalahi profile. The horizons colored in light-pink and light- cyan represent zones of desorption and re-adsorption of Li as inferred in this study (detailed discussion in Section 5.4).

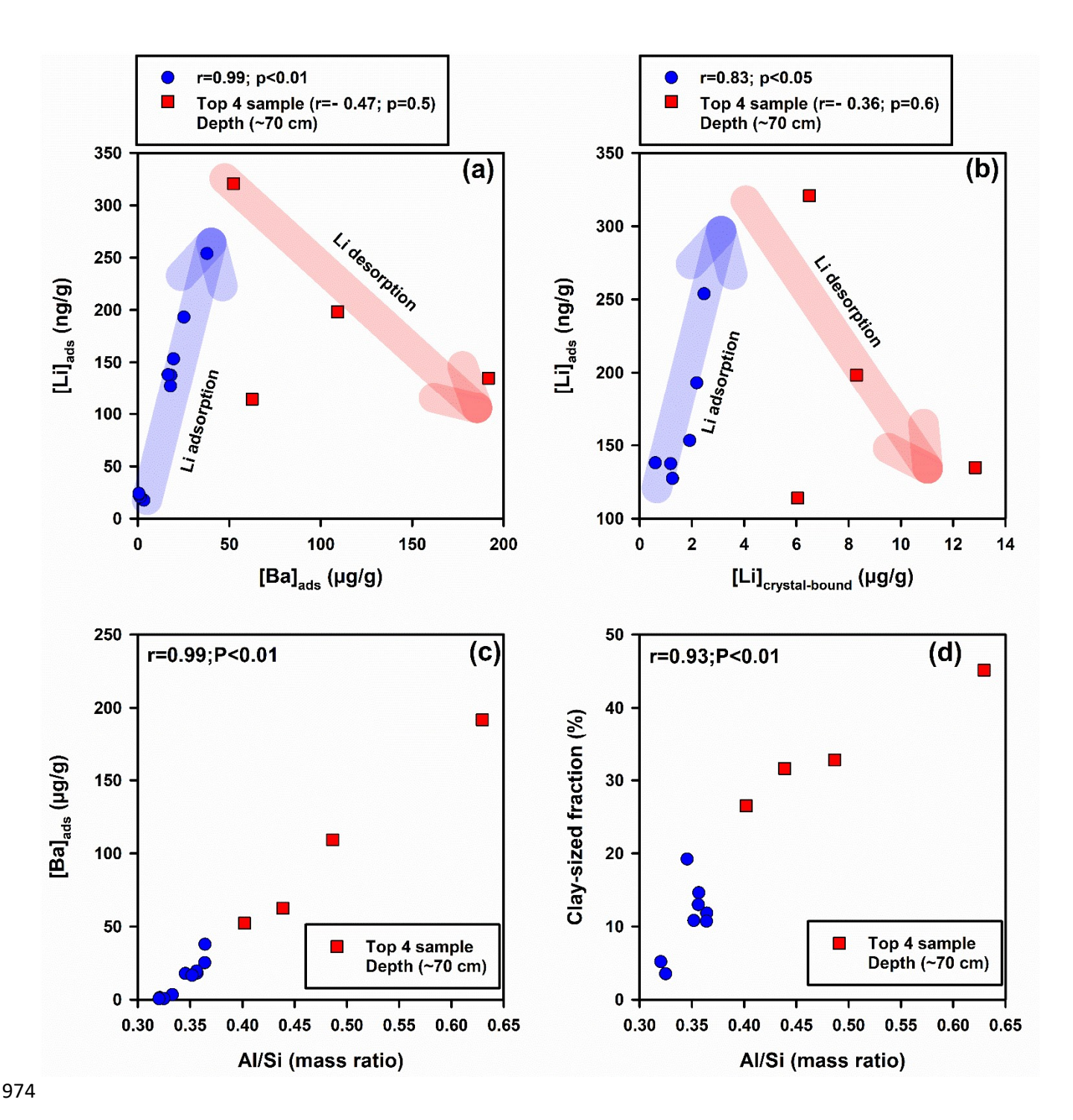


Fig. 6. Significant positive correlations of [Li]_{ads} with [Ba]_{ads} (a) and [Li]_{crystal-bound} (b) are observed in the lower section, whereas weak negative correlations are evident in the upper section of the Dalahi profile. Note that degree of Ba adsorption keeps increasing with abundances of clay minerals, as evident from a positive correlation of [Ba]_{ads} and clay-sized fractions with Al/Si (c, d) ratio in the profile. Together, these observations are suggestive of Li adsorption in the profile, except in the upper horizon where its desorption is evident. The arrows colored in light-blue and light-red represent the direction of increasing adsorption and desorption of Li, respectively.

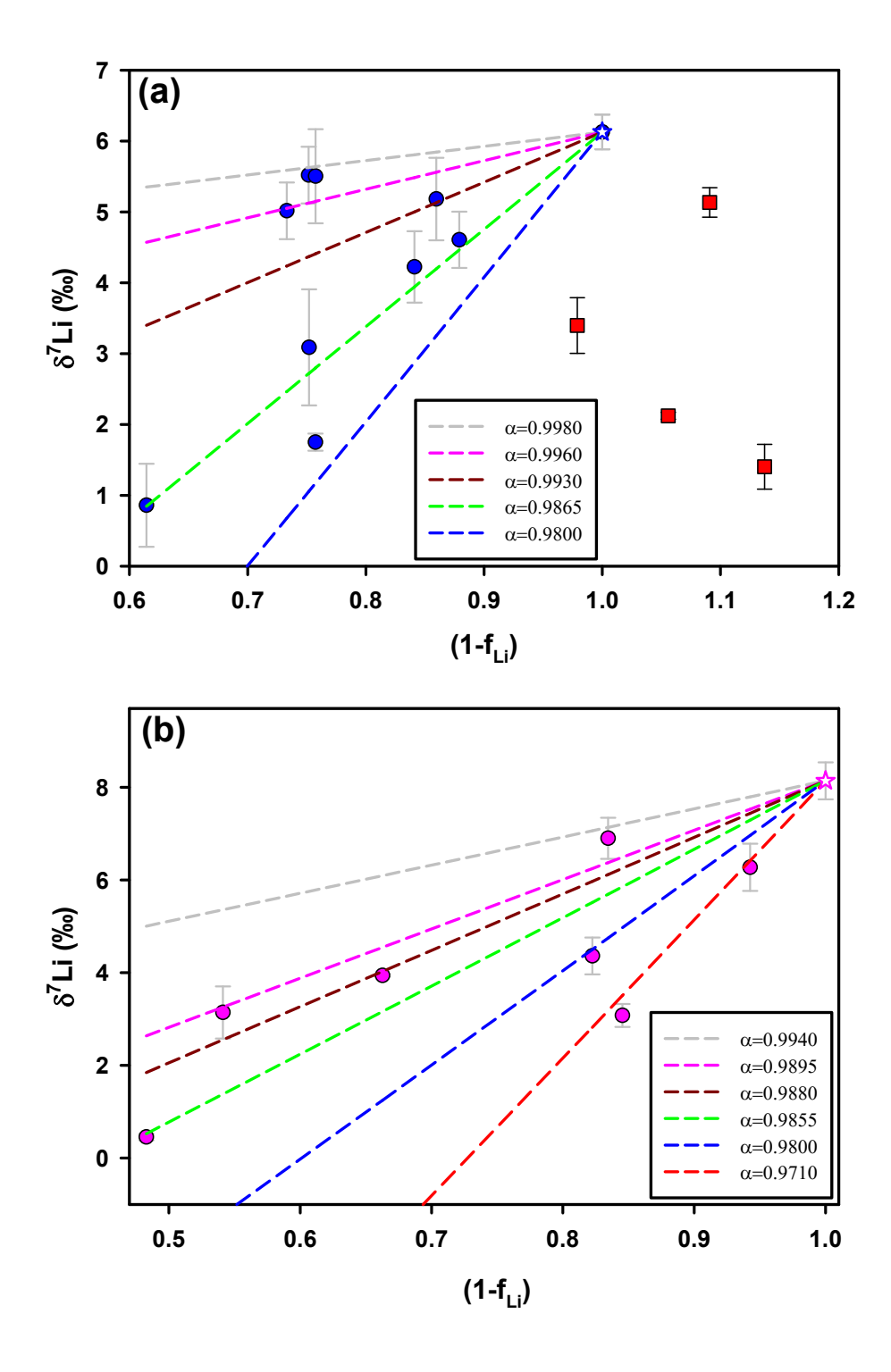


Fig. 7. $\delta^7 \text{Li}$ of weathered basalts as a function of proportion of Li incorporated into secondary phases (1- f_{Li}) in Dalahi (a) and Pakuria profile (b). Straight lines represent the evolution of $\delta^7 \text{Li}$ predicted by the batch fractionation model (see section 5.5). The circles represent the measured $\delta^7 \text{Li}$ as a function of calculated (1- f_{Li}) values. The four samples (square) in the upper section of the Dalahi profile are outside the model prediction because of inferred desorption of Li (see section 5.4, Fig. 6). Stars represent the parent basalt $\delta^7 \text{Li}$.

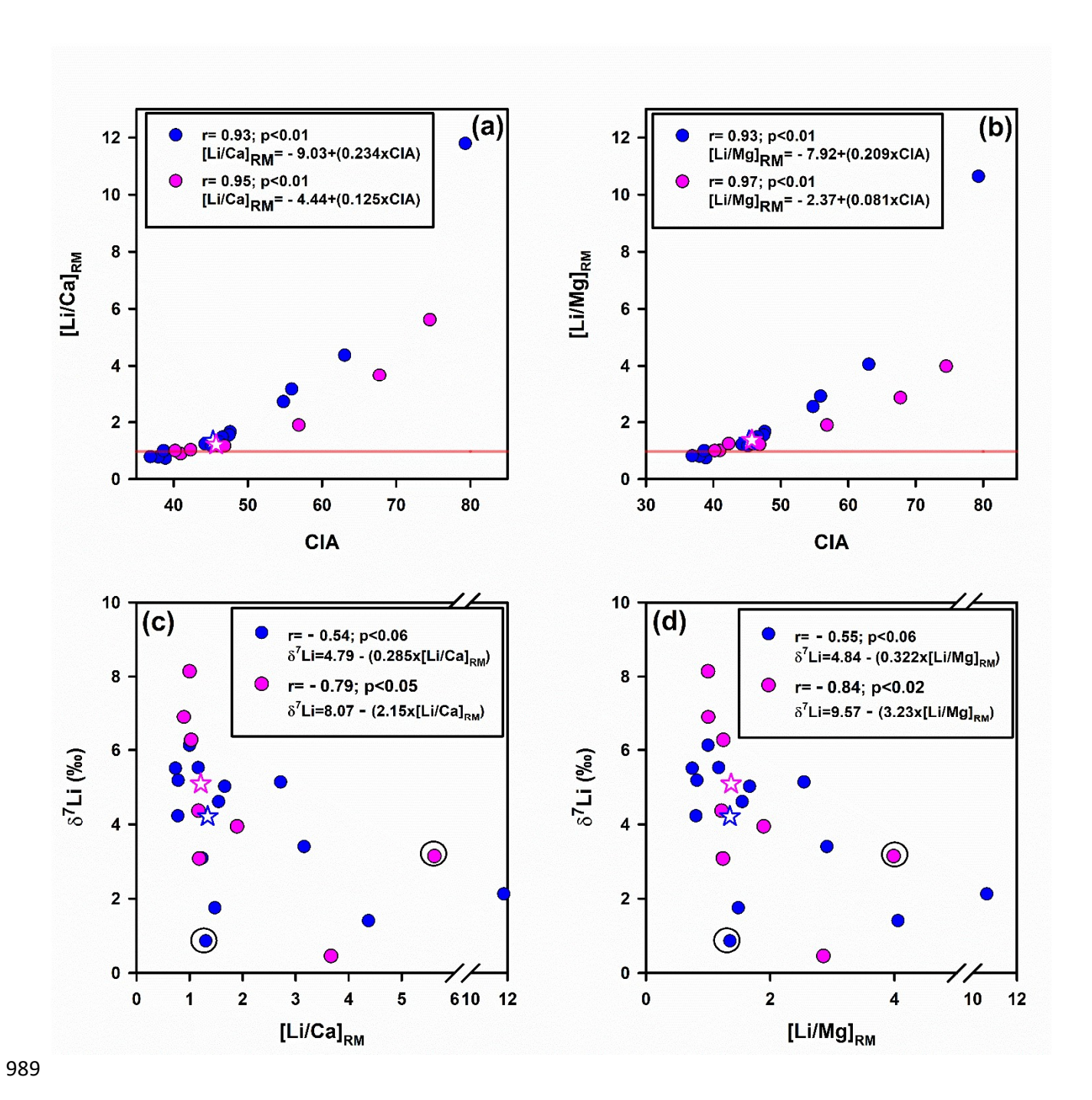


Fig. 8. Variation of $\left(\frac{\text{Li}}{\text{Ca}}\right)_{\text{RM}}$ (a) and $\left(\frac{\text{Li}}{\text{Mg}}\right)_{\text{RM}}$ (b) as a function of CIA in the studied profiles. The variation of $\delta^7\text{Li}$ with $\left(\frac{\text{Li}}{\text{Ca}}\right)_{\text{RM}}$ (c) and $\left(\frac{\text{Li}}{\text{Mg}}\right)_{\text{RM}}$ (d) are also shown. The stars represent the whole-profile values, determined based on mass balance calculations (section 5.7). The outliers (open-circled) are excluded from regression analysis. Dalahi profile (blue), Pakuria profile (pink).

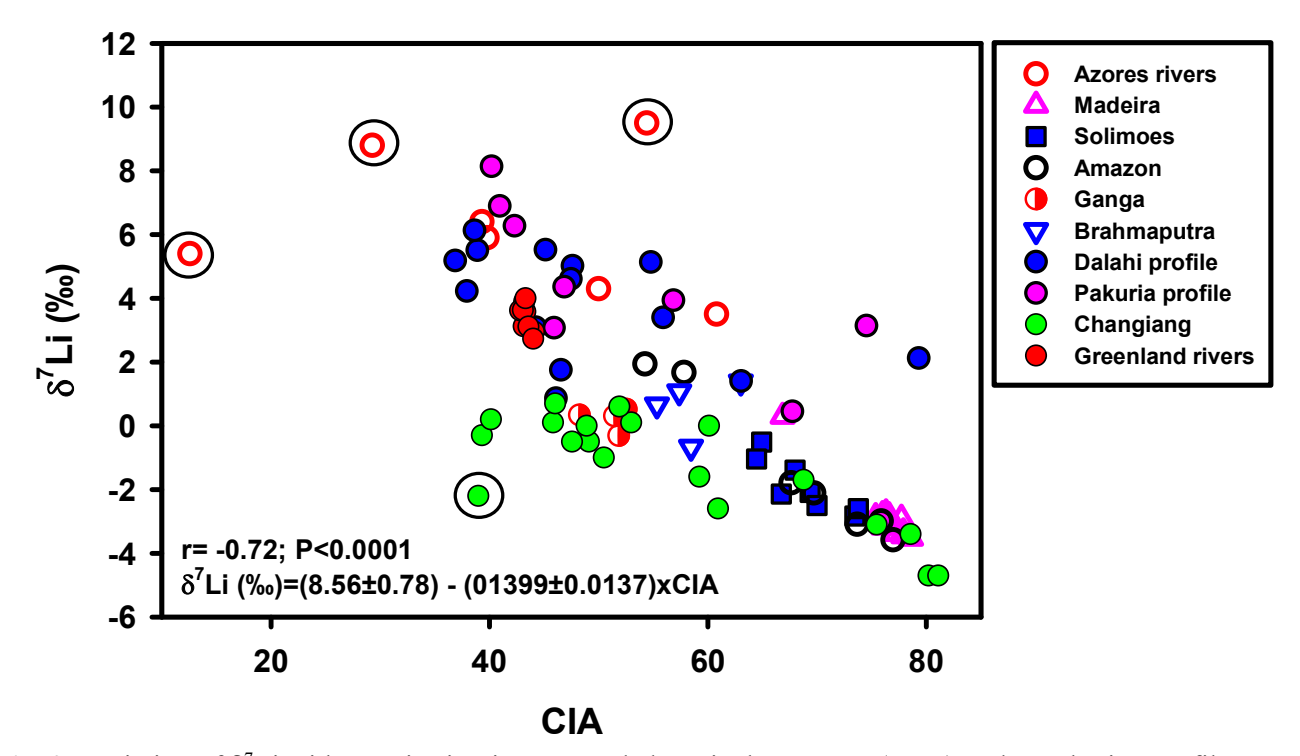


Fig. 9. Variation of δ^7 Li with CIA in riverine suspended particulate matter (SPM) and weathering profiles of this study. A few outliers (circled) are excluded from regression analysis. δ^7 Li data sources: Azores rivers (Pogge von Strandmann et al., 2010), Madeira (Dellinger et al., 2014), Solimoes (Dellinger et al., 2014), Amazon (Dellinger et al., 2014), Ganga (Dellinger et al., 2014), Brahmaputra (Dellinger et al., 2014), Changjiang (Wang et al., 2015), and Greenland rivers (Wimpenny et al., 2010b). CIA values of SPM were calculated using major element oxides data from Pogge von Strandmann et al. (2010) for the Azores rivers, Bouchez et al. (2011) for the Maderia, Solimoes and Amazon, Lupker et al. (2013) for the Ganga and Brahmaputra, Chetelat et al. (2009) for the Changjiang, and Wimpenny et al. (2010b) for the Greenland rivers. CIA values are calculated as [Al₂O₃×100/(Al₂O₃+K₂O+CaO+Na₂O)], where oxides are in molar proportions (Nesbitt and Young, 1982).

Tables

Table 1. Major and trace element concentrations, and Li isotopic composition of the weathered and parent basalts.

Sample code	Depth (cm)	pН	Density (g/cm³)	Al	Ca	Fe	Mg	Na	K	Si	Mn	Al/Si	CIA	Li	Th	Cs	δ ⁷ Li (‰)	$2\sigma^{a}$
	` ′		(g/cm)				wt. %	6				mass ratio			μg/g			
Dalahi pro	ofile (DP)																	
RJS 3	32	6.59	1.30	11.2	1.63	14.3	0.96	0.55	0.12	17.8	0.35	0.63	79	14.45	2.14	0.75	2.12	0.05
RJS 4	43	6.84	1.66	9.97	3.40	12.5	1.96	1.01	0.12	20.5	0.35	0.49	63	11.19	1.54	0.43	1.40	0.32
RJS 5	53	6.79	2.08	9.53	4.67	10.1	2.67	1.27	0.12	21.7	0.22	0.44	55	9.55	1.37	0.31	5.14	0.21
RJS 6	66	7.23	1.97	8.98	4.17	10.6	2.42	1.16	0.15	22.3	0.33	0.40	56	9.91	1.58	0.44	3.40	0.39
RJS 7	78	7.33	2.11	8.41	5.43	8.48	2.89	1.52	0.22	23.1	0.26	0.36	48	6.78	1.45	0.37	5.02	0.59
RJS 8	87	7.10	1.97	8.43	5.53	9.05	2.95	1.52	0.13	23.1	0.21	0.36	47	6.44	1.15	0.21	4.61	0.40
RJS 9	99	7.39	2.14	8.33	6.27	8.69	3.36	1.68	0.13	23.3	0.18	0.36	44	5.80	1.21	0.22	3.09	0.40
RJS 10	110	7.09	2.20	8.35	5.67	9.07	3.00	1.58	0.15	23.5	0.18	0.36	47	6.29	1.30	0.29	1.75	0.82
RJS 11	124	6.81	2.11	8.25	5.70	8.53	2.94	1.57	0.19	23.9	0.15	0.35	46	5.59	1.42	0.35	0.86	0.12
RJS 12	235	7.07	2.08	8.30	5.97	8.84	3.17	1.68	0.14	23.6	0.19	0.35	45	5.21	1.09	0.17	5.52	0.66
RJS 13	247	7.14	2.25	7.89	7.45	7.98	3.91	1.93	0.14	23.7	0.13	0.33	39	4.11	0.85	0.07	5.51	0.50
RJS 14	269	6.84	2.25	7.82	7.63	8.41	3.94	2.05	0.17	24.4	0.14	0.32	38	4.46	0.83	0.06	4.23	0.58
RJS 15	296	7.30	2.25	7.76	7.64	8.27	3.91	2.45	0.20	23.9	0.13	0.32	37	4.51	0.82	0.08	5.18	0.40
RJS 16 (parent)	376	8.05	2.26	7.70	7.17	8.37	3.83	2.02	0.32	24.0	0.14	0.32	39	5.39	0.84	0.06	6.13	0.24
Pakuria p	rofile (PP))																
PB1	90	7.30	1.65	9.91	2.02	8.67	1.10	0.47	0.16	20.4	0.19	0.49	75	9.61	24.0	0.46	3.14	0.07
PB2	125	7.46	2.10	9.49	4.15	7.31	1.60	1.25	0.22	22.4	0.11	0.42	57	6.65	13.0	0.19	3.94	0.56
PB3	165	7.22	1.70	9.17	2.49	8.55	1.23	0.75	0.20	21.1	0.19	0.43	68	7.72	18.4	0.41	0.45	0.03
PB4	225	7.44	2.20	9.00	6.13	7.46	2.25	1.84	0.28	23.2	0.12	0.39	46	6.13	12.0	0.09	3.08	0.40
PB5	290	7.36	2.10	8.76	5.81	7.76	2.15	1.67	0.22	22.9	0.10	0.38	47	5.74	12.7	0.08	4.36	0.44
PERN	325	7.63	2.30	8.67	7.14	7.46	2.44	2.31	0.27	23.5	0.12	0.37	41	5.38	11.9	0.04	6.90	0.25
PFAA	625	8.09	2.61	9.30	7.00	6.59	2.23	2.58	0.34	24.0	0.10	0.39	42	6.10	12.3	0.07	6.27	0.51
PFB1 (parent)	1000	8.42	2.58	8.71	7.40	7.40	2.85	2.42	0.22	23.3	0.12	0.37	40	6.26	11.9	0.02	8.14	0.40

Depth, pH, density, major element, Th and Cs concentrations, and CIA values are from Sharma et al. (2025).

^b 2σ represents the external 2 standard deviation of duplicate measurements for each sample (See subsection 3.2.1).

Table 2. Major and trace element concentrations in the exchangeable and oxyhydroxide phases, and clay-sized fractions in the profiles. The relative mobility parameters are also listed.

Dalahi profile (DP) RJS 3 32 45.2 40.8 4.99 175 5.73 183 992 270 17.16 129 7.37 1 RJS 4 43 32.8 16.2 3.50 89.6 6.83 95.6 1138 190 19.60 191 5.12 4 RJS 5 53 31.6 26.1 4.34 52.4 9.10 94.0 550 328 10.05 105 5.65 22 RJS 6 66 26.5 14.0 1.62 34.6 17.8 122.1 1115 211 17.59 303 7.57 3 RJS 7 78 11.8 8.34 0.99 24.2 19.4 104.8 787 131 13.55 234 5.12 1 RJS 8 87 10.7 15.0 1.41 19.7 24.7 67.54 487 134 5.46 168 3.09 1 RJS 9 99	$\left(\frac{i}{a}\right)_{RM}^{a} = \left(\frac{Li}{Mg}\right)_{RM}^{a}$	1 / Li \ 🧿		liucs	yhydrox	UX			able	change	Ex		Clay-sized	Sample code Depth	
Dalahi profile (DP) RJS 3 32 45.2 40.8 4.99 175 5.73 183 992 270 17.16 129 7.37 1 RJS 4 43 32.8 16.2 3.50 89.6 6.83 95.6 1138 190 19.60 191 5.12 4 RJS 5 53 31.6 26.1 4.34 52.4 9.10 94.0 550 328 10.05 105 5.65 2 RJS 6 66 26.5 14.0 1.62 34.6 17.8 122.1 1115 211 17.59 303 7.57 3 RJS 7 78 11.8 8.34 0.99 24.2 19.4 104.8 787 131 13.55 234 5.12 1 RJS 8 87 10.7 15.0 1.41 19.7 24.7 67.54 487 134 5.46 168 3.09 1 RJS 9 99	17 RM (Mg/RM	$\left(\frac{2\pi}{G_2}\right)$	Cs	Li	Ba	Al	Mn	Cs	Li	Ba	Al	Mn	fraction	(cm)	
RJS 3 32 45.2 40.8 4.99 175 5.73 183 992 270 17.16 129 7.37 1 RJS 4 43 32.8 16.2 3.50 89.6 6.83 95.6 1138 190 19.60 191 5.12 4 RJS 5 53 31.6 26.1 4.34 52.4 9.10 94.0 550 328 10.05 105 5.65 22 RJS 6 66 26.5 14.0 1.62 34.6 17.8 122.1 1115 211 17.59 303 7.57 RJS 7 78 11.8 8.34 0.99 24.2 19.4 104.8 787 131 13.55 234 5.12 1 RJS 8 87 10.7 15.0 1.41 19.7 24.7 67.54 487 134 5.46 168 3.09 1 RJS 9 99 14.6 9.66 6.91 14.6 27.8 75.57 298 216 3.46 110 3.58 RJS 10 110 13.0 20.9 1.81 16.3 26.4 79.16 309 147 3.18 127 3.15 1		(Ca) RM	g/g	ng		μg/g		g/g	n		μg/g		(%)		
RJS 4 43 32.8 16.2 3.50 89.6 6.83 95.6 1138 190 19.60 191 5.12 4 RJS 5 53 31.6 26.1 4.34 52.4 9.10 94.0 550 328 10.05 105 5.65 2 RJS 6 66 26.5 14.0 1.62 34.6 17.8 122.1 1115 211 17.59 303 7.57 RJS 7 78 11.8 8.34 0.99 24.2 19.4 104.8 787 131 13.55 234 5.12 RJS 8 87 10.7 15.0 1.41 19.7 24.7 67.54 487 134 5.46 168 3.09 RJS 9 99 14.6 9.66 6.91 14.6 27.8 75.57 298 216 3.46 110 3.58 RJS 10 110 13.0 20.9 1.81 16.3 26.4 79.16 309 147 3.18 127 3.15														P)	Dalahi profile (D
RJS 5 53 31.6 26.1 4.34 52.4 9.10 94.0 550 328 10.05 105 5.65 2 RJS 6 66 26.5 14.0 1.62 34.6 17.8 122.1 1115 211 17.59 303 7.57 3 RJS 7 78 11.8 8.34 0.99 24.2 19.4 104.8 787 131 13.55 234 5.12 1 RJS 8 87 10.7 15.0 1.41 19.7 24.7 67.54 487 134 5.46 168 3.09 1 RJS 9 99 14.6 9.66 6.91 14.6 27.8 75.57 298 216 3.46 110 3.58 1 RJS 10 110 13.0 20.9 1.81 16.3 26.4 79.16 309 147 3.18 127 3.15 1	1.79 10.64	11.79	7.37	129	17.16	270	992	183	5.73	175	4.99	40.8	45.2	32	RJS 3
RJS 6 66 26.5 14.0 1.62 34.6 17.8 122.1 1115 211 17.59 303 7.57 3 RJS 7 78 11.8 8.34 0.99 24.2 19.4 104.8 787 131 13.55 234 5.12 1 RJS 8 87 10.7 15.0 1.41 19.7 24.7 67.54 487 134 5.46 168 3.09 1 RJS 9 99 14.6 9.66 6.91 14.6 27.8 75.57 298 216 3.46 110 3.58 1 RJS 10 110 13.0 20.9 1.81 16.3 26.4 79.16 309 147 3.18 127 3.15 1	4.38 4.06	4.38	5.12	191	19.60	190	1138	95.6	6.83	89.6	3.50	16.2	32.8	43	RJS 4
RJS 7 78 11.8 8.34 0.99 24.2 19.4 104.8 787 131 13.55 234 5.12 1 RJS 8 87 10.7 15.0 1.41 19.7 24.7 67.54 487 134 5.46 168 3.09 1 RJS 9 99 14.6 9.66 6.91 14.6 27.8 75.57 298 216 3.46 110 3.58 1 RJS 10 110 13.0 20.9 1.81 16.3 26.4 79.16 309 147 3.18 127 3.15 1	2.72 2.55	2.72	5.65	105	10.05	328	550	94.0	9.10	52.4	4.34	26.1	31.6	53	RJS 5
RJS 8 87 10.7 15.0 1.41 19.7 24.7 67.54 487 134 5.46 168 3.09 1 RJS 9 99 14.6 9.66 6.91 14.6 27.8 75.57 298 216 3.46 110 3.58 1 RJS 10 110 13.0 20.9 1.81 16.3 26.4 79.16 309 147 3.18 127 3.15	3.16 2.91	3.16	7.57	303	17.59	211	1115	122.1	17.8	34.6	1.62	14.0	26.5	66	RJS 6
RJS 9 99 14.6 9.66 6.91 14.6 27.8 75.57 298 216 3.46 110 3.58 1 RJS 10 110 13.0 20.9 1.81 16.3 26.4 79.16 309 147 3.18 127 3.15 1	1.66 1.67	1.66	5.12	234	13.55	131	787	104.8	19.4	24.2	0.99	8.34	11.8	78	RJS 7
RJS 10 110 13.0 20.9 1.81 16.3 26.4 79.16 309 147 3.18 127 3.15 1	1.55 1.55	1.55	3.09	168	5.46	134	487	67.54	24.7	19.7	1.41	15.0	10.7	87	RJS 8
	1.23 1.23	1.23	3.58	110	3.46	216	298	75.57	27.8	14.6	6.91	9.66	14.6	99	RJS 9
	1.48 1.49	1.48	3.15	127	3.18	147	309	79.16	26.4	16.3	1.81	20.9	13.0	110	RJS 10
RJS 11 124 19.2 22.9 1.83 15.4 37.1 123.7 232 240 2.41 90.2 6.48 1	1.30 1.35	1.30	6.48	90.2	2.41	240	232	123.7	37.1	15.4	1.83	22.9	19.2	124	RJS 11
RJS 12 235 10.8 15.2 6.57 12.5 24.4 69.3 388 134 4.04 114 2.92 1	1.16 1.17	1.16	2.92	114	4.04	134	388	69.3	24.4	12.5	6.57	15.2	10.8	235	RJS 12
RJS 13 247 nm 6.38 11.3 2.84 6.98 30.1 19.7 167 0.44 10.6 1.88 0	0.73 0.75	0.73	1.88	10.6	0.44	167	19.7	30.1	6.98	2.84	11.3	6.38	nm	247	RJS 13
RJS 14 269 nm 1.50 6.25 1.07 8.19 14.6 3.15 174 0.20 12.4 1.64 0	0.78 0.81	0.78	1.64	12.4	0.20	174	3.15	14.6	8.19	1.07	6.25	1.50	nm	269	RJS 14
RJS 15 296 3.53 2.75 11.6 0.47 10.4 27.0 8.51 155 0.13 12.5 2.47 (0.79 0.82	0.79	2.47	12.5	0.13	155	8.51	27.0	10.4	0.47	11.6	2.75	3.53	296	RJS 15
RJS 16 (parent) 376 5.18 1.80 10.6 0.44 9.05 19.2 6.91 163 0.11 14.9 1.98 1	1.00 1.00	1.00	1.98	14.9	0.11	163	6.91	19.2	9.05	0.44	10.6	1.80	5.18	376	RJS 16 (parent)
Pakuria profile (PP)														PP)	Pakuria profile (l
PB1 90 20.5 4.57 2.55 73.37 15.6 41.9 829 116 12.6 160 2.63 5	5.62 3.99	5.62	2.63	160	12.6	116	829	41.9	15.6	73.37	2.55	4.57	20.5	90	PB1
PB2 125 13.6 9.75 2.49 36.24 16.5 57.0 298 155 1.56 44.1 1.76 1	1.89 1.90	1.89	1.76	44.1	1.56	155	298	57.0	16.5	36.24	2.49	9.75	13.6	125	PB2
PB3 165 15.1 2.98 5.82 30.24 29.3 70.0 780 81.9 10.28 125 3.27 3	3.67 2.86	3.67	3.27	125	10.28	81.9	780	70.0	29.3	30.24	5.82	2.98	15.1	165	PB3
PB4 225 4.42 6.84 2.78 16.15 10.1 33.6 147 206 0.60 17.4 0.88 1	1.18 1.24	1.18	0.88	17.4	0.60	206	147	33.6	10.1	16.15	2.78	6.84	4.42	225	PB4
PB5 290 5.55 5.71 7.30 15.00 9.85 34.2 156 239 0.60 19.3 1.21 1	1.17 1.22	1.17	1.21	19.3	0.60	239	156	34.2	9.85	15.00	7.30	5.71	5.55	290	PB5
PERN 325 nm 2.46 15.1 5.74 5.11 16.8 82.8 190 0.92 9.74 0.84 0	0.89 1.00	0.89	0.84	9.74	0.92	190	82.8	16.8	5.11	5.74	15.1	2.46	nm	325	PERN
PFAA 625 5.22 0.87 25.4 4.62 5.31 28.0 15.1 274 0.49 9.87 1.50 1	1.03 1.25	1.03	1.50	9.87	0.49	274	15.1	28.0	5.31	4.62	25.4	0.87	5.22	625	PFAA
PFB1 (parent) 1000 nm 6.11 14.9 0.37 29.2 5.03 10.4 178 0.06 23.3 0.59 1	1.00 1.00	1.00	0.59	23.3	0.06	178	10.4	5.03	29.2	0.37	14.9	6.11	nm	1000	PFB1 (parent)

nm: not measured

The Mn concentrations in the exchangeable and oxyhydroxide phases are from Sharma et al. (2025).

^aSee eq. 13 for determination of $\left(\frac{\text{Li}}{\text{Ca}}\right)_{\text{RM}}$ and $\left(\frac{\text{Li}}{\text{Mg}}\right)_{\text{RM}}$.

Table 3. Results of the calculated mass flux of Li derived from parent basalts and aeolian dust source.

Profile Name	Profile thickness (cm)	Collapse factor (Sc)	F _{Li} ^{basalt} a (mg/cm ²)	F _{Li} ^{dust} b (mg/cm ²)	(f _{Li} ^{dust}) ^c ×100 (%)
Dalahi profile (DP)	376	2.54	11.65	0.13	1.12
Pakuria profile (PP)	1000	2.84	45.76	0.26	0.58

 $^{{}^{\}mathbf{a}}_{F_{Li}}^{basalt}$ is calculated using eq. 3.

 $^{{}^{\}mathbf{b}}_{F_{Li}^{dust}}$ is calculated using eq. 2.

 $[\]label{eq:flux} \begin{tabular}{l} c f_{Li}^{dust} is calculated as: f_{Li}^{dust} = $\frac{F_{Li}^{dust}}{F_{Li}^{basalt}}$. \end{tabular}$

1004	Supplementary information for
1005 1006	A lithium isotopic perspective of basalt weathering: Cycling of Li and its mobility relative to Ca and Mg
1007	
1008 1009	Anup Kumar Sharma ^{1*} , Tarun Kumar Dalai ¹ , Sambuddha Misra ² , Prem Chand Kisku ³ , Jitendra Kumar Pattanaik ⁴
1010	
1011 1012	¹ Department of Earth Sciences, Indian Institute of Science Education and Research Kolkata, Mohanpur 741246, India
1013	² Centre for Earth Sciences, Indian Institute of Science, Bangalore 560012, India
1014 1015	³ Council of Scientific and Industrial Research-National Geophysical Research Institute (CSIR-NGRI), Uppal Road, Hyderabad 500007, India
1016	⁴ Department of Geology, Central University of Punjab, Bathinda, Punjab 151401, India
1017	*Corresponding author: Anup Kumar Sharma (ak.sharma20795@gmail.com)
1018	
1019	
1020	
1021	
1022	
1023	
1024	
1025	
1026	
1027	The Supplementary information include:
1028	1. Section S1. Processing of samples
1029 1030	 Section S2: Previously published data Section S3: Estimation of crystal-bound elemental concentration in neo-formed clay minerals
1030	 4. Section S4: Calculation of δ⁷Li_{crystal-bound}
1032	5. Section S5: Calculation of CIA and mobility of Li relative to Ca and Mg for whole profiles
1033	6. Figures: Fig. S1 to Fig. S10.
1034	7. Tables: Table S1 to Table S4.
1035	
1036	

Section S1. Processing of samples

S1.1 Preparation of glass beads for determination of major elements concentration by XRF

Major element concentrations were determined by analyzing the fusion beads (glass beads). The powdered samples were accurately weighed and mixed with a flux of 65% lithium tetraborate (Li₂B₄O₇) and 35% lithium metaborate (LiBO₂) in a 1:10 ratio, and a few grains of lithium bromide were added to the mixture. The mixtures were transferred into platinum crucibles and melted at 1250° C. The melts were poured into pre-heated platinum moulds to form the fusion beads. The beads were removed and stored in desiccator for at least twenty-four hours before analysis.

S1.2 Sample dissolution

About 100 mg of accurately weighed dry sample powders were combusted at 550°C in a muffle furnace for ~5 hours to oxidize the organic matter. The ashed samples were quantitively dissolved in a mixture of HNO₃, HCl and HF in a 1:3:2 volume ratio in a pre-cleaned PFA vial (Savillex®). The digested samples were subsequently evaporated to dryness at sub-boiling temperature (~80°C) and then gravimetrically re-dissolved in ~60 g of 5% HNO₃. Procedural blanks, sample replicates and certified reference standards were processed with every batch of digestion. The HNO₃ and HCl used for sample processing were double distilled (DD) in a Savillex® DST-1000 sub-boiling distillation unit, whereas the ultrapure grade HF was procured commercially.

S1.3 Sequential extraction

The exchangeable and amorphous Fe-Mn oxyhydroxide phases were extracted following the established methods (Gupta and Chen, 1975; Chen et al., 2012) detailed in Sharma et al. (2025). Briefly, the extraction of exchangeable phases involved leaching of ~3 g of powdered sample in pre-cleaned 50 mL centrifuge tube with 40 mL of 1N ammonium acetate (Sigma Aldrich, > 99.99 % purity) buffered at pH 7 with superpure ammonium hydroxide (Carlo Erba). These mixtures were shaken on a reciprocating

shaker overnight at 400 rpm and were subsequently centrifuged at 5000 rpm. The supernatants were decanted into pre-cleaned Savillex[®] beakers. The residues were washed three times with Milli-Q water (18.2 MΩ-cm) and washings were collected and mixed with the supernatant. The leachates were dried and gravimetrically re-dissolved in 5% HNO₃ prior to analysis. For extraction of oxyhydroxide phases, the residues left after the extraction of exchangeable phases were treated with 40 mL of 0.005N hydroxylamine hydrochloride (HH; 99.999% purity); 1.5% acetic acid (≥99.99% purity) and 0.03N ethylenediaminetetraacetic acid (EDTA; 99.995% purity) solution, buffered at pH 4 with sodium hydroxide. The mixtures were shaken for one hour on a reciprocating shaker at 400 rpm, and then processed as outlined above for exchangeable fractions.

Section S2. Previously published data

Major element concentrations were determined using glass beads by a Bruker® Tiger S-8 WD-X-Ray Spectrometer. Analytical accuracy was evaluated through repeated analyses of certified reference standards NIST 2711a (soil), SDC-1 (mica schist), and MESS-3 (marine sediment), and was better than ±8% (~0.3-7% for Al, ~2-4% for Ca, ~4-6% for Mg, ~0.6-6% for Si, ~3-5% for Na, ~0.6-3% for K, ~1-8% for Fe and ~0.3-4% for Mn). Based on the analysis of samples in replicates, the analytical reproducibility was within ±5%.

The concentrations of Th and Cs were measured by a triple quadrupole inductively coupled plasma mass spectrometer (QQQ-ICP-MS; Agilent® 8900) at IISc, Bangalore. Based on the analysis of certified reference standards BCR-2 (basalt), BHVO-2 (basalt), and GSP-2 (granodiorite), the measurement accuracy was better than ± 4 (~3 for Cs and ~1-3.5% for Th). Analytical reproducibility, determined from replicate analyses of samples, was within $\pm 3\%$.

The concentrations of Mn in the exchangeable and oxyhydroxide fractions were determined using a quadrupole ICP-MS (ThermoScientific® X Series 2) at IISER Kolkata. Based on the analysis of certified reference standard BHVO-2 and NIST-traceable standard IV-Stock 8 (Inorganic Ventures®), the measurement accuracy was \sim 0.5-2.7%. Analytical reproducibility, based on replicate analyses, was within \pm 7% for both phases.

Section S3. Estimation of crystal-bound Li concentration in neo-formed clay minerals

We deconvolute and quantify elemental budgets of three distinct pools of weathered materials; (i) adsorbed (interlayer sites; [X]_{ads}), (ii) crystal-bound (crystal structure of neo-formed minerals; [X]_{crystal-bound}), and (iii) residual silicate minerals ([X]_{Res}), representing the unweathered or primary minerals. Clay minerals incorporate trace elements into two primary sites: the octahedral site (or crystal-bound) and the interlayer site (adsorbed). Thus total (bulk) elemental concentration within the weathering profile can be written in terms of the contribution from the above three components as:

1093
$$[X]_{total} = [X]_{Res} + [X]_{crystal-bound} + [X]_{ads}$$
 S1

where $[X]_{Res}$, $[X]_{crystal-bound}$ and $[X]_{ads}$ represent elemental concentration in the residual silicate minerals, crystal structure of clay minerals and adsorbed phases (exchangeable + oxyhydroxides), respectively, per unit mass of bulk phase. We calculate [X] in the residual silicate minerals as:

[X]_{Res}=
$$\left(\frac{x}{Na}\right)_{parent} \times [Na]_{sample}$$
 S2

where, X represents element Li, Si or Al. As Na is a mobile element and insignificantly participates in solid-solution interaction after weathering (Gislason et al., 1996; Millot et al., 2010; Pogge von

Strandmann et al., 2017), all Na remaining in the weathered material is assumed to be residual. Therefore, we use the $\left(\frac{X}{Na}\right)_{parent}$ ratio of fresh basalts to estimate $[X]_{Res}$.

We determine elemental concentrations in the adsorbed phases by combing concentrations in the exchangeable and oxyhydroxide phases. Using the elemental concentrations of the adsorbed and residual silicate phases, per unit mass of bulk phase in eq. S1, the crystal-bound elemental concentration are calculated. These calculations show that up to ~85% and ~90% of the total Li in the Pakuria and Dalahi profiles (Table S3), respectively, is incorporated into the crystal structure of neo-formed minerals. The strong positive correlations between [Li]_{crystal-bound} and the clay-sized fractions and a near-zero y-intercept of the regression line (Fig. S10) further corroborate the reliability of our approach of estimation of Li incorporated into the crystal structure of clay minerals.

To calculate the amount of Si incorporated into the crystal structure of newly formed clay minerals, we assumed that after weathering the released Si is partitioned into: (i) the crystal structure of newly formed clay minerals, (ii) dissolved phases ([Si]_{ads}=0; Middelburg et al., 1988; Frings et al., 2021) and (iii) residual silicate minerals. Therefore, [Si]_{crystal-bound} can be calculated using equations S1 and S2.

Section S4. Calculation of δ⁷Li_{crystal-bound}

We determine the δ^7 Li value of crystal-bound Li (δ^7 Li_{crystal bound}) in neo-formed clay minerals, based on the premise that bulk Li is distributed between the residual silicate minerals, adsorbed and crystal-bound phases in secondary minerals. Therefore, the following relationship can be written:

$$\delta^7 \text{Li}_{\text{bulk}} = f_{\text{Res}} \delta^7 \text{Li}_{\text{Res}} + f_{\text{crystal-bound}} \delta^7 \text{Li}_{\text{crystal-bound}} + f_{\text{ads}} \delta^7 \text{Li}_{\text{ads}}$$
 S3

where the subscripts bulk, Res, crystal-bound, and ads represent bulk, residual silicate minerals, crystal-bound, and adsorbed phases, respectively, and f represents the fraction of Li relative to bulk Li.

The release of Li during dissolution of the parent rock is known to cause negligible Li isotope fractionation
(Pistiner and Henderson, 2003). Therefore,

$$\delta^7 \text{Li}_{\text{Res}} = \delta^7 \text{Li}_{\text{parent}}$$
 S4

By substituting eq. S4 into eq. S3, we get:

1125
$$\delta^7 \text{Li}_{\text{bulk}} = f_{\text{Res}} \delta^7 \text{Li}_{\text{parent}} + f_{\text{crystal-bound}} \delta^7 \text{Li}_{\text{crystal-bound}} + f_{\text{ads}} \delta^7 \text{Li}_{\text{ads}}$$
 S5

Previous studies have reported that the δ^7 Li of the adsorbed phases is up to 28% higher than that of crystal-bound Li in neo-formed minerals (Tong et al., 2021; Cai et al., 2024). Therefore, the relationship between δ^7 Li of the crystal-bound and adsorbed phases can be expressed as:

$$\delta^7 Li_{ads} = \delta^7 Li_{crystal-bound} + 28\%_0$$
 S6

Substituting eq. S6 into eq. S5 and rearranging gives:

1132

1133

1134

1135

1131
$$\delta^{7} \text{Li}_{\text{crystal-bound}} = \frac{\left(\delta^{7} \text{Li}_{\text{bulk}} - f_{\text{Res}} \delta^{7} \text{Li}_{\text{parent}} - 28 f_{\text{ads}}\right)}{\left(f_{\text{crystal-bound}} + f_{\text{ads}}\right)}$$
S7

Section S5. Calculation of CIA and mobility of Li relative to Ca and Mg for whole profiles

The proportion of an element (X) in a weathering profile relative to the parent rock is calculated utilizing the depth integrated mass balance of the whole profile (See eq. 10). The mobility of Li relative to Ca and Mg can be written as:

1136
$$\left(\frac{\text{Li}}{\text{X}}\right)_{\text{RM}} = \frac{f_{\text{profile}}^{\text{Li}}}{f_{\text{profile}}^{\text{X}}} = \frac{\left[\frac{\left(\sum_{i=1}^{n}[\text{Li}]_{i}\times\Delta t_{i}\times\rho_{i}}{\sum_{i=1}^{n}[\text{Th}]_{i}\times\Delta t_{i}\times\rho_{i}}\right)}{\left(\frac{\text{Li}}{\text{Th}}\right)_{p}}\right]}{\left[\frac{\left(\sum_{i=1}^{n}[\text{X}]_{i}\times\Delta t_{i}\times\rho_{i}}{\sum_{i=1}^{n}[\text{Th}]_{i}\times\Delta t_{i}\times\rho_{i}}\right)}{\left(\frac{\text{X}}{\text{Th}}\right)_{p}}\right]}$$
S8

where ρ_i and Δt_i represent the density and thickness of any sampling section (i), respectively, and X is the elemental concentration of Ca or Mg. Based the eq. S8, the mobility of Li relative to Ca and Mg, is calculated to be 1.34 and 1.35 for the Dalahi profile, and 1.21 and 1.37 for the Pakuria profile, respectively. Using eq. 11 (details in the section 5.6 of main text), we calculated the depth-integrated δ^7 Li values of the whole profiles to be 4.21% for the Dalahi profile and 5.07% for the Pakuria profile. These δ^7 Li values of the weathered material are 1.92% and 3.07% lower than those of the parent material in the Dalahi and Pakuria profiles, respectively. Using eq. 10, we calculated the fraction of each element/oxide in the weathering profile relative to the parent rock. To determine the depth integrated CIA value for the whole profile, we calculated concentrations of Al₂O₃, CaO, Na₂O, and K₂O for the whole profile. This was done by multiplying the element fractions in the weathering profile relative to the parent rock by the elemental concentrations of the parent rock. The CIA values were then calculated using the molar proportions of these oxides as (Nesbitt and Young, 1982):

1149
$$CIA = \left[\frac{Al_2O_3}{(Al_2O_3 + CaO + Na_2O + K_2O)} \right] \times 100$$
 S9

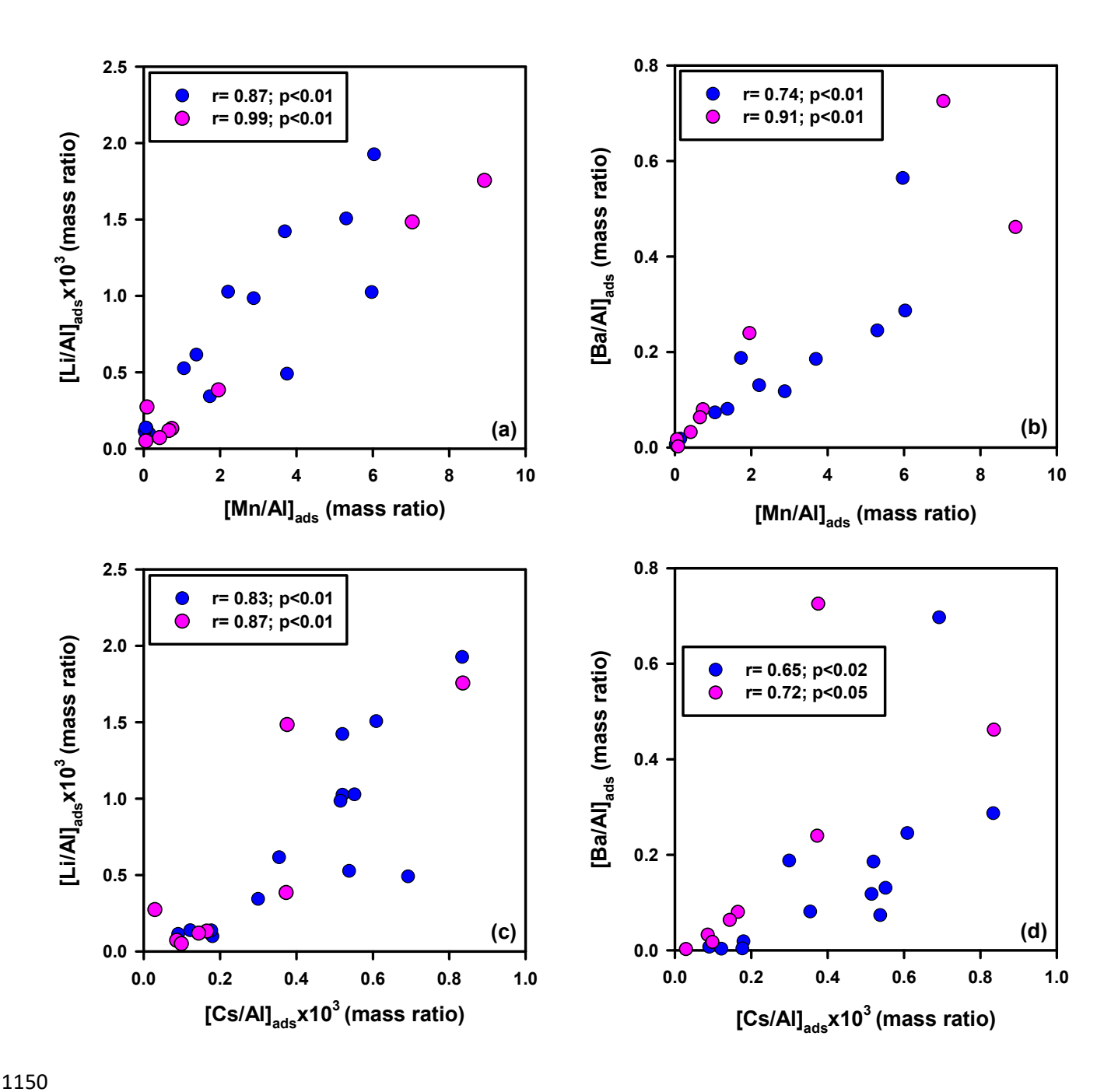


Fig. S1. Significant positive correlations of [Li/Al]_{ads} (a, c) and [Ba/Al]_{ads} (b, d) with [Mn/Al]_{ads} and [Cs/Al]_{ads} in the Dalahi (blue) and Pakuria (pink) profiles.

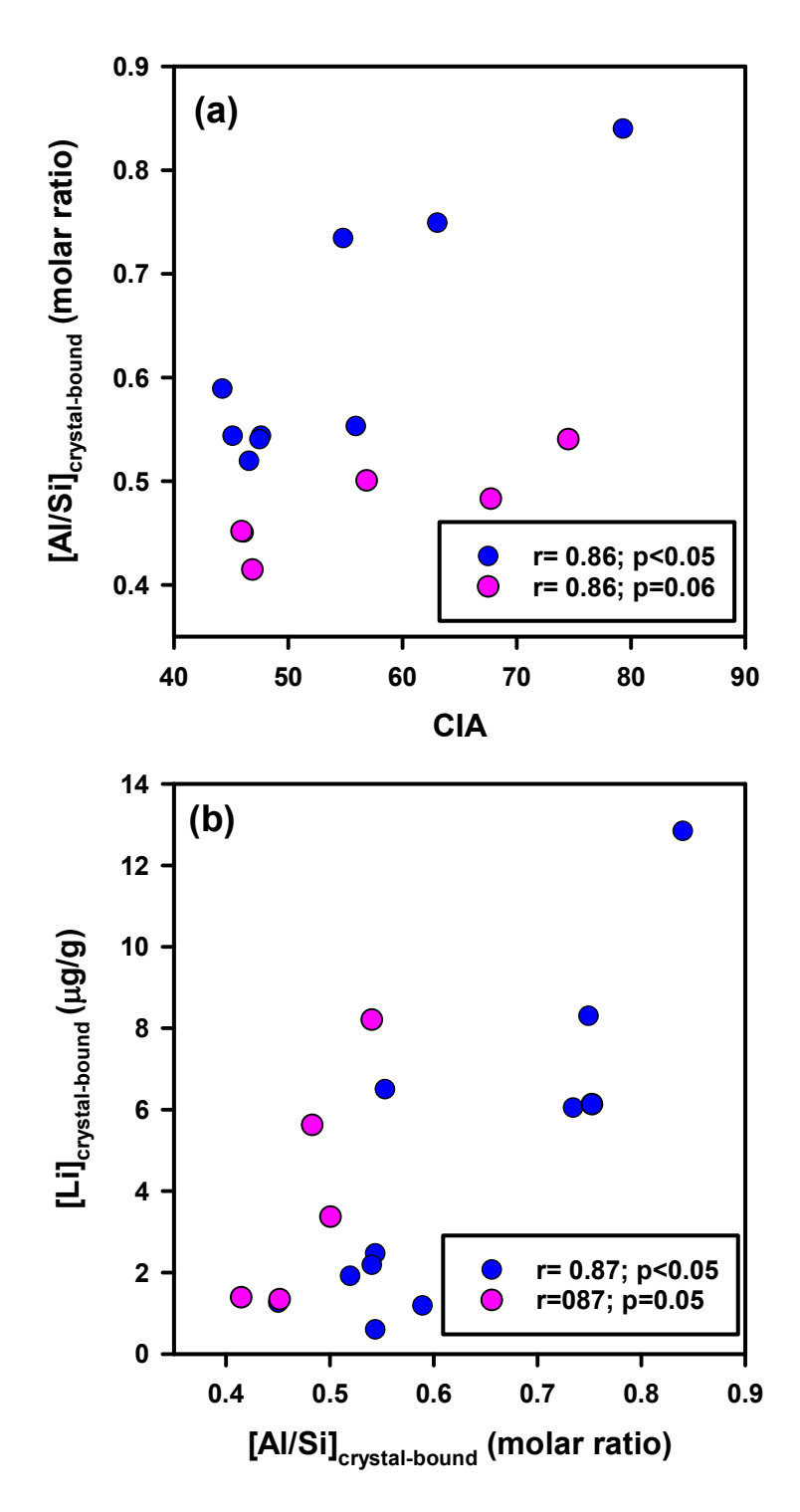


Fig. S2. The positive correlation of [Al/Si]_{crystal-bound} with CIA (a) and [Li]_{crystal-bound} (b) in the Dalahi (blue) and Pakuria profile (pink). See Section S3 and Table S3 for details on the calculation of crystal-bound elemental concentrations in newly formed clay minerals. Note: four fresh basalt samples from the Dalahi and three from Pakuria profiles, with CIA values ≤42, are excluded in these plots (See Table S3 for details).

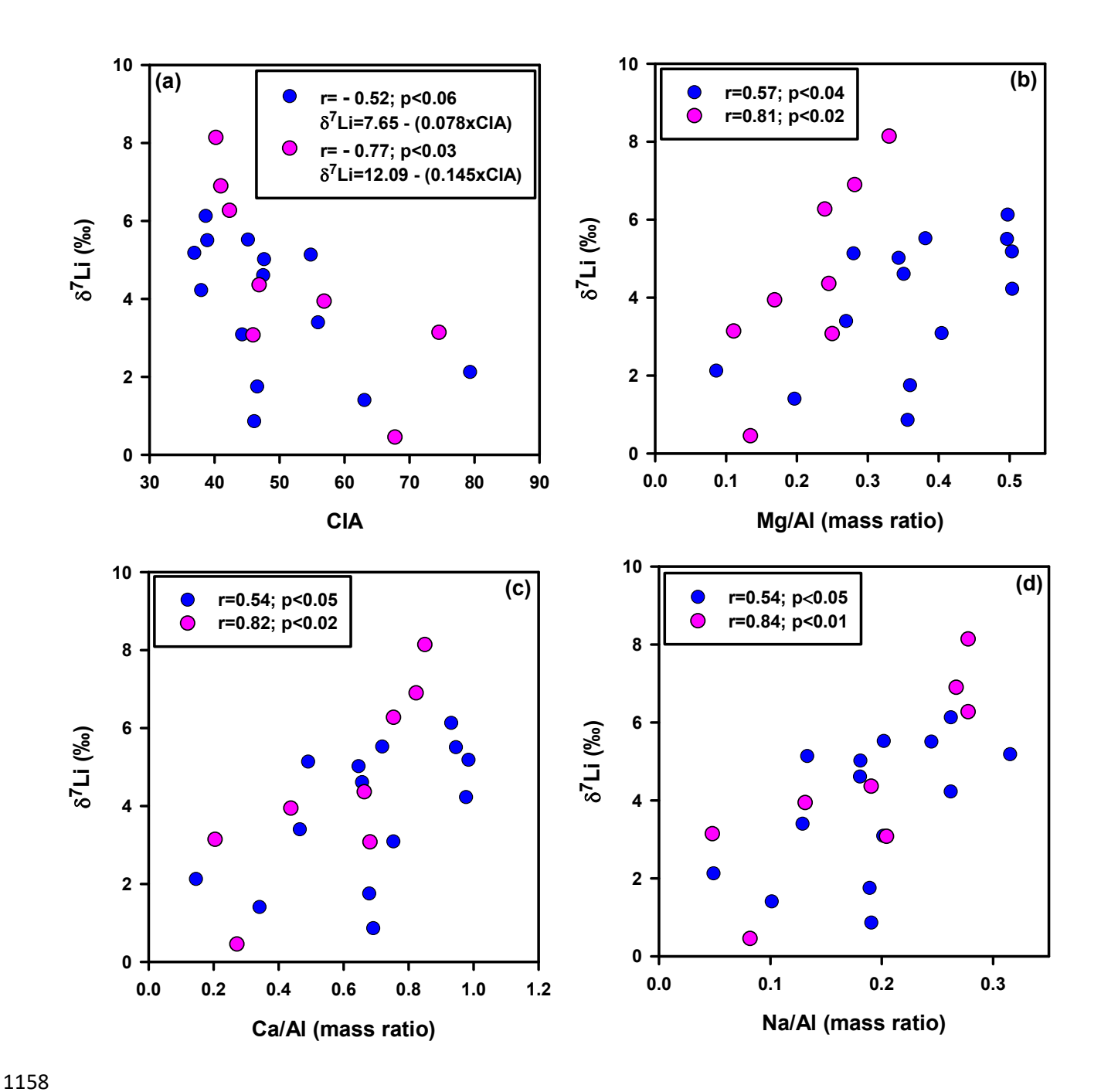


Fig. S3. The δ^7 Li values of weathered material as a function of CIA (a), Mg/Al (b), Ca/Al (c) and Na/Al (d) in the Dalahi (blue) and Pakuria profile (pink).

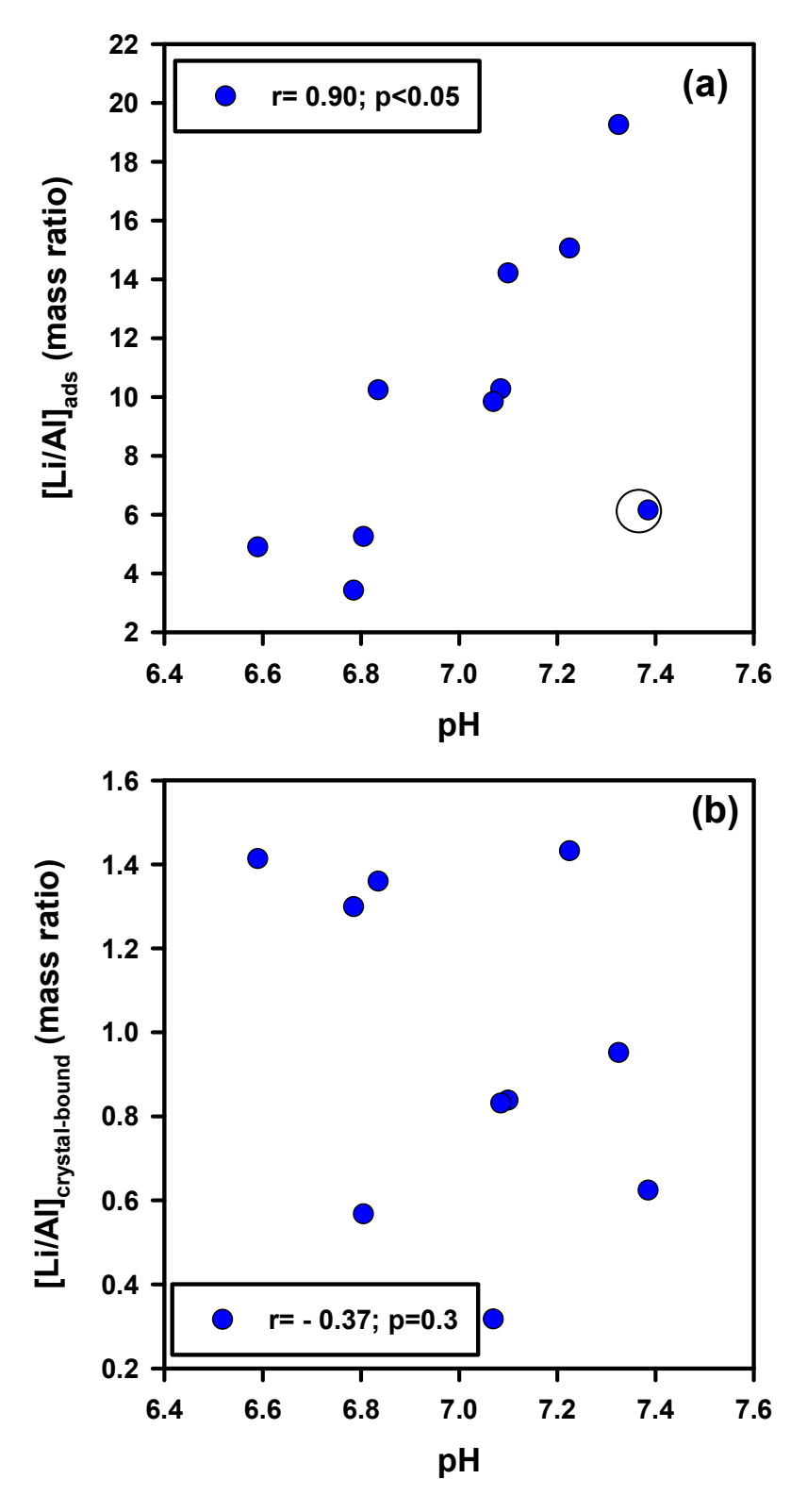


Fig. S4. The [Li/Al]_{ads} show a positive correlation with pH, whereas [Li/Al]_{crystal-bound} show no systematic trend with pH in the Dalahi profile. The outlier (circled) is excluded from regression analysis. Note: four fresh basalt samples are excluded from panel **b** (see Table S3 for details).

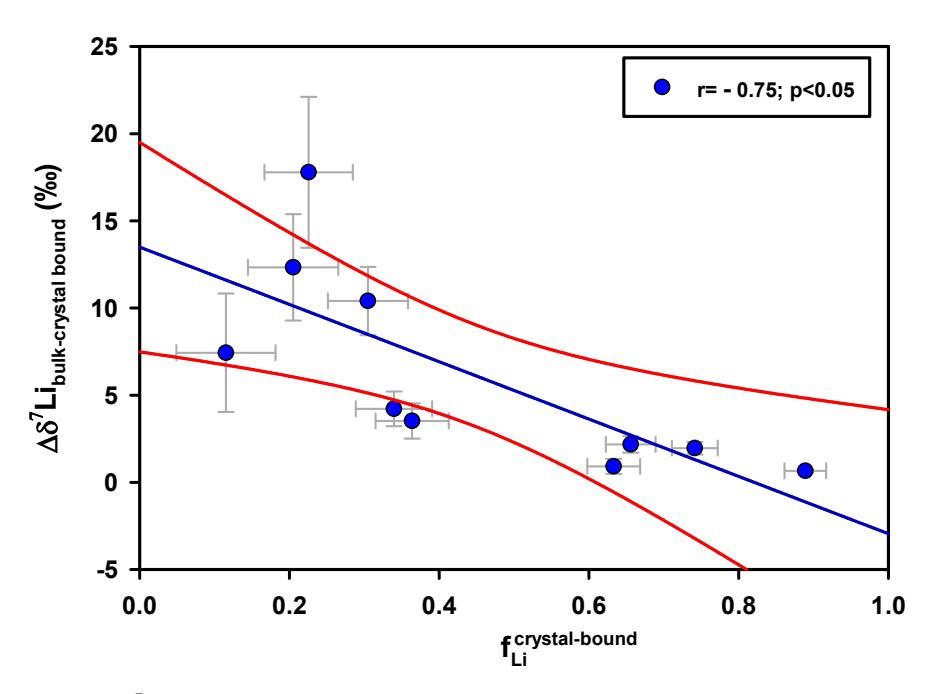


Fig. S5. Variation of $\Delta \delta^7 \text{Libulk-crystal bound}$ as a function of fraction of Li in the crystal structure (Section S4) of neoformed clay minerals in the Dalahi profile. Note: four fresh basalt samples with chemical index of alteration (CIA) values ≤ 39 (Table 1) are excluded in this plot (See Table S3 for details). The line of regression (blue) and 95% confidence intervals (red) are also shown.

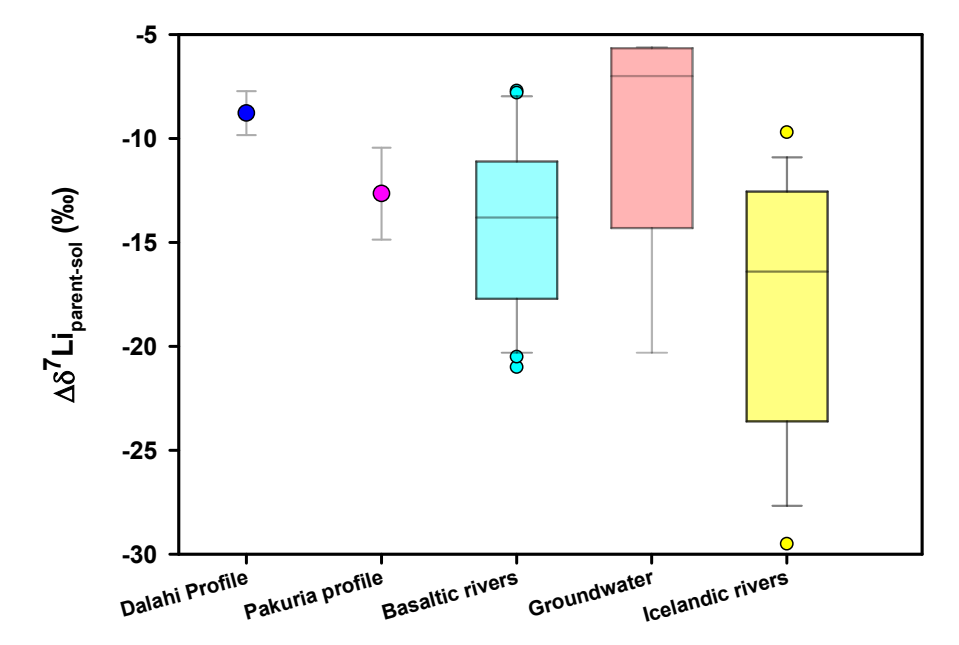


Fig. S6. Comparison of $\Delta\delta^7 Li_{parent-sol}$ values in two weathering profiles of this study with $\Delta\delta^7 Li_{parent-sol}$ values reported for present-day groundwater (Liu et al., 2015) and river water draining basaltic catchments (Pogge von Strandmann et al., 2006; Liu et al., 2015). Our calculated $\Delta\delta^7 Li_{parent-sol}$ values are bracketed by those determined in the basaltic catchments. The parent $\delta^7 Li$ value for Iceland basalt was taken from Marschall et al. (2024).

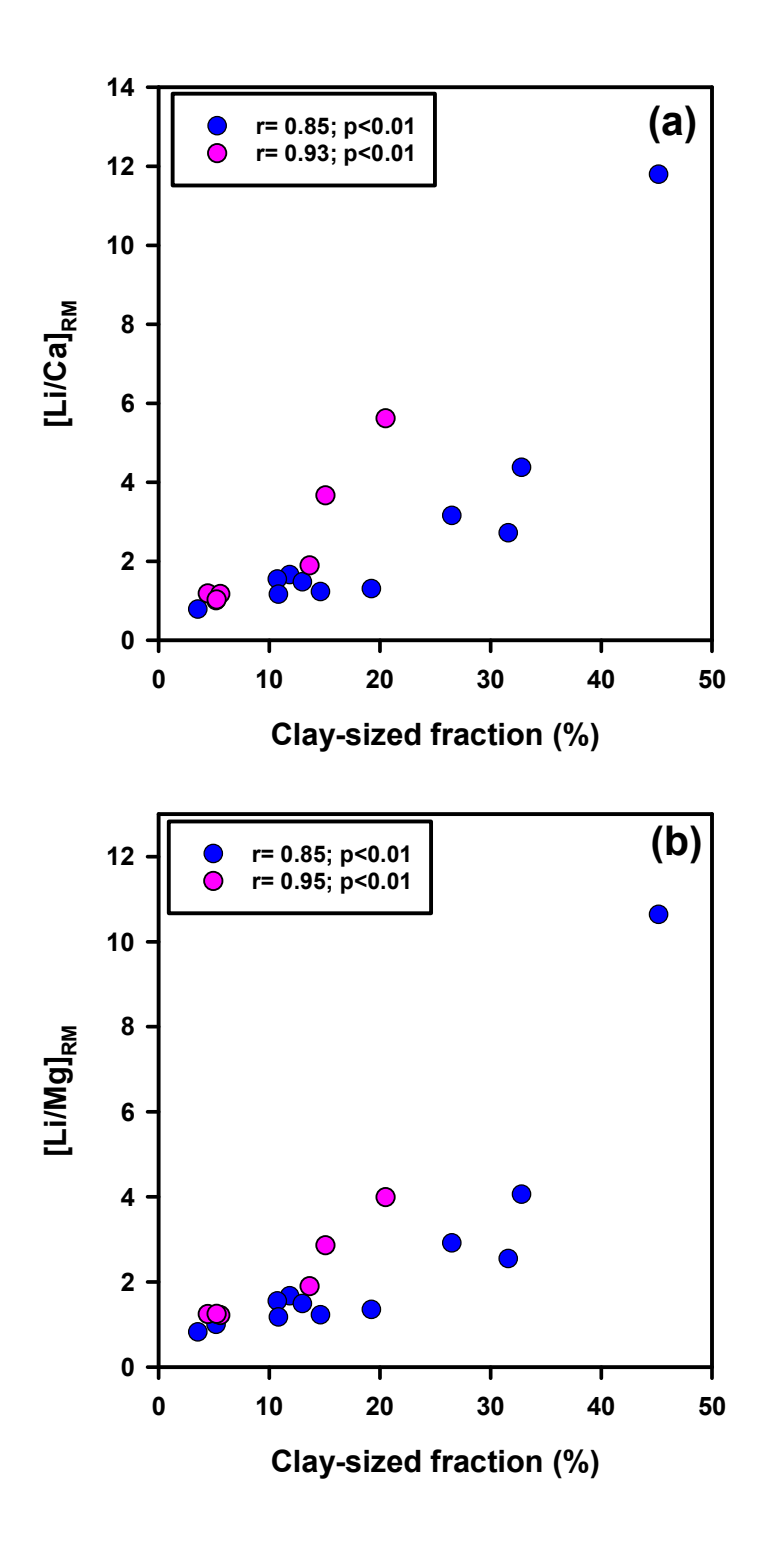


Fig. S7. Significant positive correlations of $\left(\frac{\text{Li}}{\text{Ca}}\right)_{\text{RM}}$ (a) and $\left(\frac{\text{Li}}{\text{Mg}}\right)_{\text{RM}}$ (b) with clay-sized fraction (%) in the Dalahi (blue) and Pakuria (pink) profile.

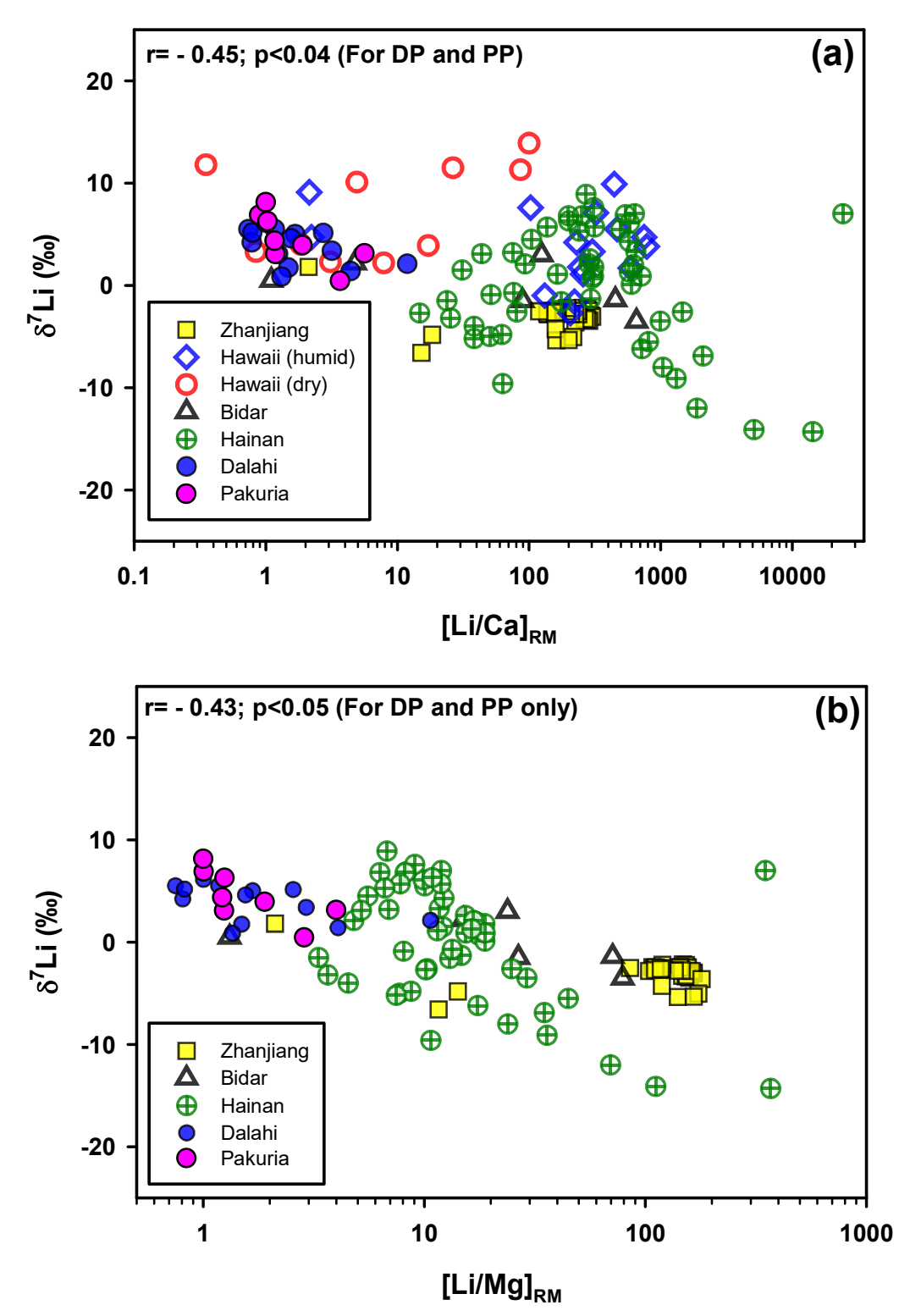


Fig. S8. δ^7 Li of weathered basalts as a function of the mobility of Li relative to Ca (a) and Mg (b) in the Dalahi, Pakuria, Hainan, Bidar, Hawaii and Zhanjiang profiles. Data sources: Zhanjiang (Tong et al., 2021), Hawaii (Li et al., 2020), Bidar (Kisakurek et al., 2004) and Hainan (Xiong et al., 2022). Note that [Li/Mg]_{RM} values for Hawaiian weathered basalts could not be determined as Mg data is not available.

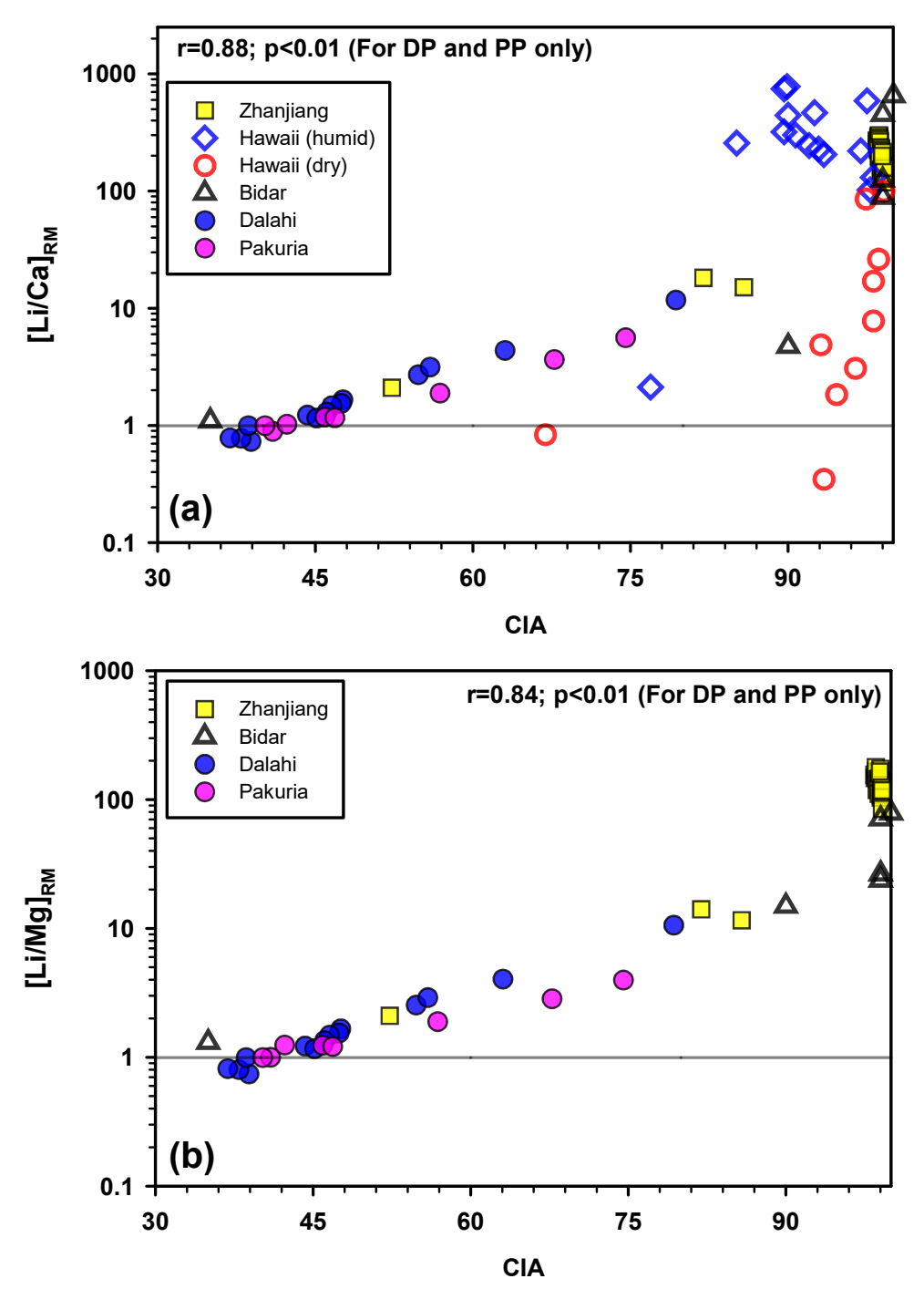


Fig. S9. Variation of relative mobility parameters vs. CIA in the weathered basalts in the Dalahi, Pakuria, Bidar, Hawaii and Zhanjiang profiles. The positive correlation of the mobility of Li relative to Ca (a) and Mg (b) with CIA suggests that as weathering intensity increases, Li becomes less mobile compared to Ca and Mg. The variation trends exhibit steeper slopes at CIA values >90. The horizontal lines represent identical mobility of Li relative to Ca and Mg. Data sources: Zhangjiang (Tong et al., 2021), Hawaii (Li et al., 2020); Hainan (Xiong et al., 2022) and Bidar (Kisakurek et al., 2004). Note that [Li/Mg]_{RM} values for Hawaiian weathered basalts could not be determined as Mg data is not available.

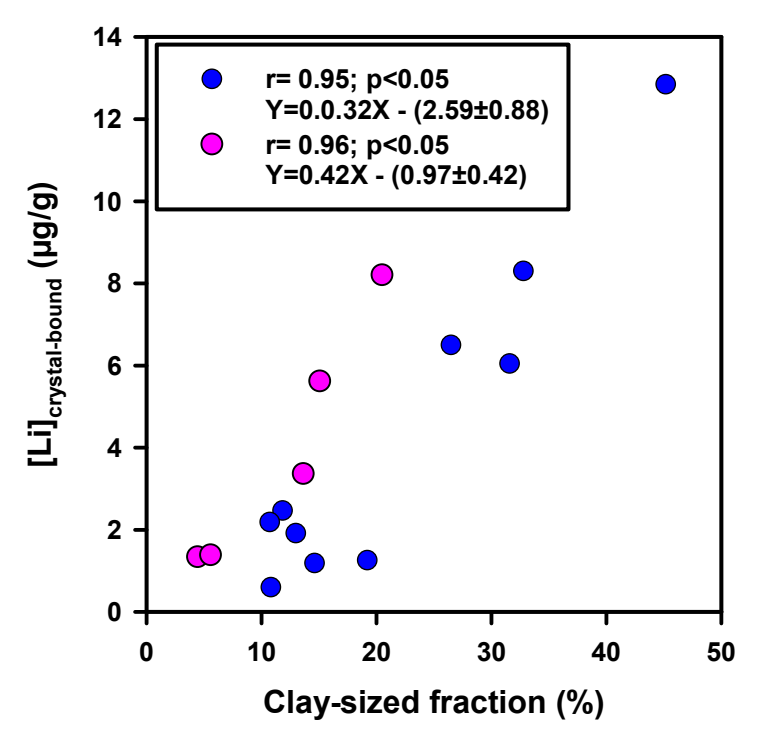


Fig. S10. The strong positive correlation between [Li]_{crystal-bound} and clay-sized fraction (%) in the Dalahi (blue) and Pakuria (pink) profile. Note: four fresh basalt samples from the Dalahi and three from Pakuria profiles are excluded in this plot (see Table S3 for details).

Table S1. The concentrations of Li in the certified reference standards during analysis of bulk samples.

Elements (μg/g)	Reference standard	Certified Value	Measured value	Accuracy (%)	n
Li	BHVO-2	5	4.9 ± 0.5	1.5	3
Li	JSD-3	151	161.3 ± 1.2	-6.8	3
Li	GSP-2	36±1	35.5	1.3	1

Table S2. Major and trace element concentrations in the reference standards during analysis of exchangeable and oxyhydroxide phases.

Elements (μg/g)	Reference standard	Certified/Reported Value	Measured value	Accuracy (%)	n
Li	BHVO-2	5	4.87 ± 0.03	2.6	3
Li	IV-Stock 8	100.1 ± 0.4	100.5 ± 2.5	-0.5	4
Al	BHVO-2	7.16 ± 0.08	6.71 ± 0.58	6.3	3
Al	IV-Stock 8	100.1 ± 0.4	99.1 ± 5.2	0.9	3
Ba	BHVO-2	130±13	128 ± 8	1.3	3
Ba	IV-Stock 8	100.1 ± 0.4	97.9 ± 7.1	2.1	4
Cs*	BHVO-2	0.0996 ± 0.002	0.093 ± 0.005	6.6	3

^{*}Reported values from Jochum et al. (2015).

Table S3. Calculated concentrations of Li, Al and Si in neo formed clay minerals and its fraction relative to bulk phase and molar [Al/Si]_{crystal-bound} ratios.

Sample	Depth	[Li]crystal-	[Al]crystal-	[Si]crystal-	[Al/Si] crystal-	$f_{Li}^{crystal-bound} \times$
Code	(cm)	bound	bound	bound	_{bound} (molar	100 (%) ^b
		μg/g	wt. %	wt. %	ratio) ^a	
Dalahi pro	ofile (DP)					
RJS-3	32	12.8	9.09	11.3	0.84	89
RJS-4	43	8.30	6.10	8.48	0.75	74
RJS-5	53	6.04	4.65	6.60	0.73	63
RJS-6	66	6.50	4.54	8.54	0.55	66
RJS-7	78	2.47	2.59	4.96	0.54	36
RJS-8	87	2.19	2.61	5.03	0.54	34
RJS-9	99	1.19	1.90	3.37	0.59	20
RJS-10	110	1.92	2.31	4.62	0.52	30
RJS-11	124	1.26	2.22	5.13	0.45	23
RJS-12	235	0.60	1.89	3.62	0.54	12
RJS-13	247	nc	nc	nc	nc	nc
RJS-14	269	nc	nc	nc	nc	nc
RJS-15	296	nc	nc	nc	nc	nc
RJS-16	376	nc	nc	nc	nc	nc
Pakuria P	rofile (PP))				
B1	90	8.21	8.19	15.8	0.54	85
PB2	125	3.37	4.98	10.4	0.50	51
PB3	165	5.62	6.46	13.9	0.48	73
PB4	225	1.34	2.35	5.43	0.45	22
PB5	290	1.39	2.72	6.83	0.41	24
PERN	325	nc	nc	nc	nc	nc
PFAA	625	nc	nc	nc	nc	nc
PFB1	1000	nc	nc	nc	nc	nc

See section S3 for the calculations of [Li]_{crystal-bound}, [Al]_{crystal-bound} and [Si]_{crystal-bound}.

nc: not calculated for four fresh basalt samples from the Dalahi (RJS-13, 14, 15 and 16) and three from the Pakuria profile (PFB1, PFAA and PERN) as their CIA values are identical to those of the parent basalts (Table 1), considering the uncertainty of estimates (Sharma et al., 2025).

^aMolar [Al/Si]_{crystal-bound} ratio = ([Al] _{crystal-bound} /[Si]_{crystal-bound}) × 1.04.

 $f_{Li}^{crystal-boun}$ is calculated as: $f_{Li}^{crystal-bound} = \frac{[Li]_{crystal-bound}}{[Li]_{bulk}}$.

Table S4. Comparison of δ^7 Li, [Li/Ca]_{RM} and [Li/Mg]_{RM} values obtained for the whole profile by mass balance calculations with those determined from regression parameters of depth-profile data.

Whole profile mass balance Input value ^a	Depth-profile data regression equation ^b	Predicted value ^c	Whole profile mass balance Calculated value ^a
Dalahi profile			
$[Li/Ca]_{RM} = 1.34$	$\delta^7 \text{Li} = (4.79 - 0.285 \times [\text{Li/Ca}]_{\text{RM}}) \%$	$\delta^7 \text{Li} = 4.4 \% \text{o}$	$\delta^7 \text{Li} = 4.2 \% \text{o}$
$[Li/Mg]_{RM} = 1.35$	$\delta^7 \text{Li} = (4.84 - 0.322 \times [\text{Li/Mg}]_{\text{RM}}) \%$	$\delta^7 \text{Li} = 4.4 \% \text{o}$	$\delta^7 \text{Li} = 4.2 \%$
CIA = 45.30	$\delta^7 \text{Li} = (7.65 - 0.078 \times \text{CIA}) \%$	$\delta^7 \text{Li} = 4.1 \%$	$\delta^7 Li = 4.2 \% o$
CIA = 45.30	$[\text{Li/Ca}]_{\text{RM}} = (-9.03 + 0.234 \times \text{CIA})$	$[Li/Ca]_{RM} = 1.57$	$[Li/Ca]_{RM} = 1.34$
CIA = 45.30	$[\text{Li/Mg}]_{\text{RM}} = (-7.92 + 0.209 \times \text{CIA})$	$[Li/Mg]_{RM} = 1.54$	$[Li/Mg]_{RM} = 1.35$
Pakuria Profile			
$[Li/Ca]_{RM} = 1.21$	$\delta^7 \text{Li} = (8.07 - 2.15 \times [\text{Li/Ca}]_{\text{RM}}) \%$	$\delta^7 \text{Li} = 5.5 \%$	$\delta^7 \text{Li} = 5.1 \%$
$[Li/Mg]_{RM} = 1.37$	$\delta^7 \text{Li} = (9.57 - 3.23 \times [\text{Li/Mg}]_{\text{RM}}) \%$	$\delta^7 \text{Li} = 5.1 \%$	$\delta^7 \text{Li} = 5.1 \%$
CIA = 45.71	$\delta^7 \text{Li} = (12.09 - (0.145 \times \text{CIA}) \%$	$\delta^7 \text{Li} = 5.5 \%$	$\delta^7 \text{Li} = 5.1 \%$
CIA = 45.71	$[\text{Li/Ca}]_{\text{RM}} = (-4.44 + 0.125 \times \text{CIA})$	$[Li/Ca]_{RM} = 1.27$	$[Li/Ca]_{RM} = 1.21$
CIA = 45.71	$[\text{Li/Mg}]_{\text{RM}} = (-2.37 + 0.081 \times \text{CIA})$	$[Li/Mg]_{RM} = 1.33$	$[Li/Mg]_{RM} = 1.37$

^a Calculated from whole profile mass balance approach (See section S5).

^b Regression equations are derived from the data shown in figures 8 and S3a.

^cPredicted values of δ^7 Li were based on the input values of [Li/Ca]_{RM}, [Li/Mg]_{RM} or CIA in the regression equations obtained from depth-profile data. Predicted values of [Li/Ca]_{RM} or [Li/Mg]_{RM} values were derived by using input values of CIA in the regression equations obtained from depth-profile data.

Supplementary references

- 1229 Cai, D., Henehan, M. J., Uhlig, D., von Blanckenburg, F., 2024. Lithium isotopes in water and regolith in
- a deep weathering profile reveal imbalances in Critical Zone fluxes. Geochimica et Cosmochimica
- 1231 Acta, 369, 213-226. https://doi.org/10.1016/j.gca.2024.01.012
- 1232 Chen, T. Y., Frank, M., Haley, B. A., Gutjahr, M., Spielhagen, R. F., 2012. Variations of North Atlantic
- inflow to the central Arctic Ocean over the last 14 million years inferred from hafnium and neodymium
- isotopes. Earth and Planetary Science Letters, 353, 82-92. https://doi.org/10.1016/j.epsl.2012.08.012
- Frings, P., Oelze, M., Schubring, F., Frick, D. A., von Blanckenburg, F., 2021. Interpreting silicon isotopes
- in the critical zone. American Journal of Science, 321(8), 1164-1203.
- https://doi.org/10.2475/08.2021.02
- Ghose, N. C., Chatterjee, N., Windley, B. F., 2017. Subaqueous Eruptive Phase of the Late Aaptian
- Rajmahal Volcanism India: Evidence from Volcaniclastic Rocks, Bentonite, Black Shales and Oolite.
- 1240 Geoscience Frontiers, 8, 809-822. https://doi.org/10.1016/j.gsf.2016.06.007
- 1241 Gíslason, S. R., Arnórsson, S., Ármannsson, H., 1996. Chemical weathering of basalt in southwest Iceland:
- effects of runoff, age of rocks and vegetative/glacial cover. American Journal of Science, 296(8), 837-
- 907. http://dx.doi.org/10.2475/ajs.296.8.837
- Jochum, K.P., Weis, U., Schwager, B., Stoll, B., Wilson, S.A., Haug, G.H., Andreae, M.O., Enzweiler, J.,
- 1245 2016. Reference values following ISO guidelines for frequently requested rock reference materials.
- Geostandards and Geoanalytical Research, 40(3), 333-350. http://dx.doi.org/10.1111/j.1751-
- 1247 908X.2015.00392.x
- 1248 Kısakürek, B., Widdowson, M., James, R. H., 2004. Behaviour of Li isotopes during continental
- weathering: the Bidar laterite profile, India. Chemical Geology, 212(1-2), 27-44
- https://doi.org/10.1016/j.chemgeo.2004.08.027
- 1251 Li, W., Liu, X. M., Chadwick, O. A., 2020. Lithium isotope behavior in Hawaiian regoliths: Soil-
- atmosphere-biosphere exchanges. Geochimica et Cosmochimica Acta, 285, 175-192.
- 1253 https://doi.org/10.1016/j.gca.2020.07.012
- Liu, X. M., Wanner, C., Rudnick, R. L., McDonough, W. F., 2015. Processes controlling δ7Li in rivers
- illuminated by study of streams and groundwaters draining basalts. Earth and Planetary Science
- Letters, 409, 212-224. https://doi.org/10.1016/j.epsl.2014.10.032
- Marshall, E. W., Halldorsson, S. A., Tian, L., Jackson, M. G., Jenner, F., Stefansson, A., 2024. The effect
- of diffusion on lithium isotope ratios in Icelandic basalts. Chemical Geology, 662, 122206.
- https://doi.org/10.1016/j.chemgeo.2024.122206
- Middelburg, J. J., van der Weijden, C. H., Woittiez, J. R., 1988. Chemical processes affecting the mobility
- of major, minor and trace elements during weathering of granitic rocks. Chemical geology, 68(3-4),
- 253-273. https://doi.org/10.1016/0009-2541(88)90025-3
- Millot, R., Vigier, N., Gaillardet, J., 2010. Behaviour of lithium and its isotopes during weathering in the
- Mackenzie Basin, Canada. Geochimica et Cosmochimica Acta, 74(14), 3897-3912.
- 1265 https://doi.org/10.1016/j.gca.2010.04.025

- Nesbitt, H. W., Young, G. M., 1982. Early Proterozoic climates and plate motions inferred from major element chemistry of lutites. *Nature*, *299*, 715-717. http://dx.doi.org/10.1038/299715a0
- Pistiner, J. S., Henderson, G. M., 2003. Lithium-isotope fractionation during continental weathering processes. Earth and Planetary Science Letters 214, 327-339. https://doi.org/10.1016/S0012-821X(03)00348-0
- Pogge von Strandmann, P. A. P., Burton, K. W., James, R. H., van Calsteren, P., Gíslason, S. R., Mokadem, F., 2006. Riverine behaviour of uranium and lithium isotopes in an actively glaciated basaltic terrain. Earth and Planetary Science Letters, 251(1-2), 134-147.
- https://doi.org/10.1016/j.epsl.2006.09.001
- Pogge von Strandmann, P. A. P., Frings, P. J., Murphy, M. J., 2017. Lithium isotope behaviour during weathering in the Ganges Alluvial Plain. Geochimica et Cosmochimica Acta, 198, 17-31. https://doi.org/10.1016/j.gca.2016.11.017
- Sharma, A. K., Dalai, T. K., Kisku, P. C., Pattanaik, J. K., Misra, S., Verma, S., Shukla, A. D., 2025.

 Release and partitioning of neodymium and its radiogenic isotope during basaltic weathering.

 Chemical Geology, 122957. https://doi.org/10.1016/j.chemgeo.2025.122957
- 1281 Tong, F., Xiao, Y., Sun, H., Wang, Y., Wan, H., Gou, L.F., Gong, Y., Huang, F., Li, D.Y., Hou, Z., 2021. 1282 Lithium isotopic features of Quaternary basaltic saprolite, Zhanjiang, China: Atmospheric input and The Environment, clav-mineral adsorption. Science of Total 785. 147235. 1283 1284 https://doi.org/10.1016/j.scitotenv.2021.147235
- Xiong, Y. W., Qi, H. W., Hu, R. Z., Xiao, Y. L., Wei, L. Y., 2022. Lithium isotope behavior under extreme tropical weathering: A case study of basalts from the Hainan Island, South China. Applied Geochemistry, 140, 105295. https://doi.org/10.1016/j.apgeochem.2022.105295